ASME Journal of Tribology
Online journal at:
https://asmedigitalcollection.asme.org/tribology

P. C. Romio[1]
Faculty of Engineering,
University of Porto,
Rua Dr. Roberto Frias,
Porto 4200-465, Portugal
e-mail: pedroromio@fe.up.pt

P. M. T. Marques
INEGI,
Campus da FEUP, Rua Dr. Roberto Frias, 400,
Porto 4200-465, Portugal
e-mail: pmarques@inegi.up.pt

C. M. C. G. Fernandes
Faculty of Engineering,
University of Porto,
Rua Dr. Roberto Frias,
Porto 4200-465, Portugal;
INEGI,
Campus da FEUP, Rua Dr. Roberto Frias, 400,
Porto 4200-465, Portugal
e-mail: cfernandes@inegi.up.pt

J. H. O. Seabra
Faculty of Engineering,
University of Porto,
Rua Dr. Roberto Frias,
Porto 4200-465, Portugal
e-mail: jseabra@fe.up.pt

A Simplified Thermal Plasto-Elastohydrodynamic Lubrication Model for Circular Contact With Real Surface Roughness

The current increase in power density, contact load, and speeds have imposed new challenges on elastohydrodynamic lubrication (EHL) contact models. To overcome possible EHL limitations under such conditions, the present work presents a unified thermal plasto-elastohydrodynamic lubrication (TPEHL) model for circular contact with real surface roughness capable to simulate the different lubrication regimes. Among the main characteristics of the proposed model, one should mention the minimal implementation changes in standard EHL models; there is no need for a preliminary assessment to verify whether thermal and plastic effects are negligible (or not) since these effects will naturally take place in the simulations, and good agreement between the predictions using the model and the experimental measurements. [DOI: 10.1115/1.4062898]

Keywords: thermal plasto-elastohydrodynamic lubrication (TPEHL), circular contact numerical modelling, real surface rough contact, deterministic model, boundary lubrication, contact mechanics, surface roughness and asperities, thermoelastohydrodynamic lubrication

1 Introduction

Many oil-lubricated mechanical components transmit power and motion through the contact of surfaces. Rolling element bearings, gears, and cam-followers are typical applications where one can see interfaces interacting with each other and with a lubricant [1]. In these machine elements, the lubrication mechanism will be considerably impacted by the high contact pressure, with an influence on surface elastic displacement and an increase in lubricant viscosity, well-known as elastohydrodynamic lubrication (EHL) [2]. Even though EHL has been intensively investigated with well-established modelling [3–7], the current increase in power density, contact load and speeds have imposed new challenges on contact models. For example, the estimated EHL pressure for certain modern power transmission devices, such as continuously variable transmissions, can be as high as 5 GPa, which, even with ideally smooth surfaces, may lead to subsurface stresses above the material yield limit and affect lubrication characteristics [8]. Under these circumstances, it is no longer valid to assume that the body's materials are perfectly elastic and thermal effects, mainly over the lubricant, start playing a significant role in the contact assessment [1,2]. In order to overcome possible EHL limitations on predicting film thickness, contact area, coefficient of friction, pressure distribution and stress fields under more realistic conditions, thermal elastohydrodynamic lubrication (TEHL) [1,9–11] and plasto-elastohydrodynamic lubrication (PEHL) [2,8,12] models started appearing to deal separately with temperature and plastification over the contact area.

The proposed TEHL models in the literature [1,9–11] aim to modify lubricant properties due to the temperature variation inside the contact. Among the approaches presented to achieve this goal, this work applies the moving heat source theory over a semi-infinite solid, as indicated by Pu et al. [11], to determine the surfaces' flash temperature and the lubricant temperature distribution that modifies its properties. As Wang et al. [10] explained, it is possible to calculate the two surfaces' temperature increase using the coefficient of friction. It is essential to note that the present work follows a standard practice in the literature, in which friction and thermal effects are calculated using a non-Newtonian fluid model. At the same time, film thickness and pressure distributions are obtained from a Newtonian fluid model. There are two points to highlight here: first, EHL film thickness is dominated by the inlet zone, where the pressure and shear strain rate are still low. As a result, the Newtonian fluid model accurately predicts EHL behavior. On the other hand, inside the contact zone, where pressure and shear strain rate are high, the sliding friction and temperature increase are dominant, demanding a non-Newtonian fluid model. A complete thermal solution with a non-Newtonian fluid model may require significant computational power. It is also worth mentioning that the moving heat source over a semi-infinite solid theory may not be accurate if the

---

[1] Corresponding author.

Contributed by the Tribology Division of ASME for publication in the Journal of Tribology. Manuscript received March 21, 2023; final manuscript received June 26, 2023; published online September 4, 2023. Assoc. Editor: Hannes Grillenberger.

surface velocities are very low. However, heat generation is usually insignificant at low speeds. Therefore, possible deviations at low velocities should not be considered [13,14].

The PEHL model used in this study relies on the approach presented by Azam et al. [12], where constitutive changes are made in the EHL model solver to obtain the pressure distribution and film thickness. The plasto-elastohydrodynamic lubrication model developed in their work is based upon the idea that the nodes that deform plastically form a plane. The plastic deformation is assumed at the nodes where the pressure reaches the average yielding pressure (p_{yield}). Once a node is under plastic deformation, the normal pressure on this node is limited to the yielding pressure. As a result, more nodes are needed to handle the load, increasing the contact area. The yielding pressure ranges from 2.3 to 2.8 times the yield strength (σ_{yield}). In alternative, one can use the material hardness to evaluate the pressure limit [12]. It is important to highlight a few aspects of the used PEHL model. In fact, one should refer to it as pseudo-perfect plastic since the contact stress was not actually calculated and compared to the σ_{yield}, but instead, the pressures were truncated based on this value. Another point is that this model does not consider the work hardening, which may lead to deviations from experimental results. Finally, the model is susceptible to the average yielding pressure (p_{yield}), and once this value ranges from 2.3 to 2.8 times the yield strength (σ_{yield}), it is necessary to calibrate the model for better predictions. On the other hand, the simplicity and relatively small changes in the EHL make this approach fast and easily implemented.

Despite the existence of several EHL models, TEHL models and PEHL models, a united approach where both effects are considered together is still scarce. In this sense, this study presents for the first time in technical literature a unified thermal plasto-elastohydrodynamic lubrication (TPEHL) model for circular contact with real surface roughness capable of simulating the different lubrication regimes, providing film thickness, contact area, coefficient of friction, and pressure distribution. This work made it possible to compare simulation results for the EHL, TEHL, PEHL and TPEHL approaches and, more importantly, showed that there are operational conditions in which the thermoplastic effects overlap, producing results that isolated models (EHL, TEHL, and PEHL) might not predict.

On the other hand, it is important to stress that one must be aware that the TEHL and PEHL models chosen here to build the TEPHL algorithm have intrinsic limitations, such as the assumption of an infinitely large volume for the thermal equilibrium calculation and ideal plastic material behavior. Therefore, the proposed TPEHL model inherits those approximations of reality and possible errors that may arise. Even so, the results and discussions presented in this study are valid as a reference for developing more improved TPEHL models, as well as the agreement between the simulated results and the experimental shows its applicability.

The following three sections provide a short but careful explanation of the EHL, TEHL, and PEHL models separately. Section 2 focuses on the unified Reynolds solution for rough contact, presenting the EHL perspective [7]. Section 3 is dedicated to showing how to calculate the flash temperature in mixed lubrication [10,11], providing the bases for the TEHL approach. Section 4 presents a simple deterministic PEHL model in mixed lubrication [12], closing the models' review. In Sec. 5, one finds the TPEHL model implemented in this work, which, despite combining existing models in the literature [7,10–12], presents a set of comparative results between EHL, TEHL, PEHL, and TPEHL models. Section 6 closes the article by comparing TPEHL model predictions and experimental results, such as, coefficient of friction, film thickness, and track contact width, providing helpful information on the contact level.

2 Elastohydrodynamic Lubrication Model

Both TEHL and PEHL models are based on adaptations of existing EHL models. In this sense, it is necessary to understand the principles involved in solving the elastic isothermal problem.

Six equations can mathematically define the EHL contact: (1) the fluid flow equation (Reynolds equation), (2) the film thickness, (3) the pressure-induced elastic displacement, (4) the load balance, (5) density as a pressure and temperature function, and (6) viscosity as a pressure and temperature function [1].

Equation (1) gives the steady-state Reynolds equation for a generic contact [15]. The terms on the left side of the equality represent the Poiseuille flow terms, while the terms on the right side represent the Couette flow terms. This particular notation allows one to employ the Reynolds equation to an elliptical contact ($R_x \neq R_y$), a circular contact ($R_x = R_y$), and a linear contact ($R_y \approx \infty$)

$$\frac{\partial}{\partial x}\left(\frac{\rho \cdot h^3}{12 \cdot \eta \cdot \mathbf{v}_e}\frac{\partial p}{\partial x}\right) + \left(\frac{R_x}{R_y}\right)^2 \cdot \frac{\partial}{\partial y}\left(\frac{\rho \cdot h^3}{12 \cdot \eta \cdot \|\mathbf{v}_e\|}\frac{\partial p}{\partial y}\right) = \\ = \left[\cos^2(\varphi_e) + \left(\frac{R_x}{R_y}\right) \cdot \sin^2(\varphi_e)\right] \\ \cdot \left[\cos(\varphi_e)\frac{\partial(\rho \cdot h)}{\partial x} + \left(\frac{R_x}{R_y}\right) \cdot \sin(\varphi_e)\frac{\partial(\rho \cdot h)}{\partial y}\right] \quad (1)$$

It is necessary to highlight the assumption of an angle in the entrainment velocity (φ_e) as a function of the angle (θ) between surface 1 velocity ($\mathbf{v}_1$) and surface 2 velocity ($\mathbf{v}_2$). Figure 1 shows a circular contact scheme demonstrating the angles' relations with the axis. This kind of generalization is necessary to better describe the experimental approach presented in Sec. 6.

One can generically write the gap between the surfaces (h) as indicated in Eq. (2) [16]. Once again, one can differentiate the elliptical contact ($R_x \neq R_y$), circular contact ($R_x = R_y$) and linear contact ($R_y \approx \infty$), and extend the solution presented in this work to other types of contact geometries. Nevertheless, given the application used in this study, the circular contact will be explored from now on

$$h(x, y) = h_0 + \frac{x^2}{2R_x} + \frac{y^2}{2R_y} + u_z(x, y) + s_1(x, y) + s_2(x, y) \quad (2)$$

For the circular contact, the pressure-induced elastic displacement is then given by Eq. (3) [16]

$$u_z(x, y) = \frac{1}{\pi \cdot E^*}\iint_A \frac{p(x', y')\, dx' dy'}{\sqrt{(x - x')^2 + (y - y')^2}} \quad (3)$$

The load balance is presented in Eq. (4) [16]

$$\iint_A p(x, y)\, dx\, dy = P \quad (4)$$

Both density (ρ) and dynamic viscosity (η) are assumed to depend on pressure and temperature. Therefore, a model for the pressure and temperature density relationship is given in Eqs. (5) and (6) [17]

$$\rho = \rho_T\left(1 + \frac{C_a \cdot p}{1 + C_b \cdot p}\right) \quad (5)$$

$$\rho_T = \rho_0 \cdot [1 + \gamma_t \cdot (T_0 - T)] \quad (6)$$

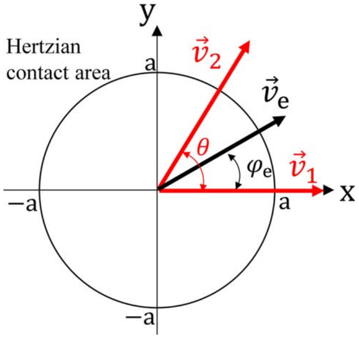

Fig. 1 Hertzian contact area and lubrication entrainment velocity

Similarly, Eqs. (7) and (8) present the well-known Barus' exponential law relating dynamic viscosity and pressure [18] and the Vogel dynamic viscosity variation with the temperature [19], respectively. These particular relations were chosen for their simplicity and wide use. As indicated in Eq. (7), the dynamic viscosity relies on the pressure-viscosity coefficient (α_{Gold}), a lubricant property. The relation between Gold's pressure-viscosity coefficient, the dynamic viscosity, and the lubricant density is shown in Eq. (9), which also depends on two oil parameters (s_G and t_G) related to oil type, pressure, and temperature [20]

$$\eta = \eta_T \cdot e^{(\alpha_{Gold} \cdot p)} \tag{7}$$

$$\eta_T = \xi \cdot e^{\left(\frac{\zeta}{T+\psi}\right)} \tag{8}$$

$$\alpha_{Gold} = s_G \cdot \left(\frac{\eta_T}{\rho_T} \times 10^3\right)^{t_G} \times 10^{-9} \tag{9}$$

It is necessary to resource numerical techniques to solve the EHL problem, in this case, the Finite Difference Method. By discretizing the problem using a rectangular grid of uniform mesh size in each direction ($\Delta x = \Delta y$), one can rewrite Eq. (1) for the circular contact ($R_x = R_y$) as indicated in Eqs. (10) and (11). It is important to note that the second-order central finite difference approach was used to discretize the Poiseuille flow terms. The first-order backward difference approach was applied to the Couette flow terms [7]. The convenient notations $\varepsilon_{i,j}^{x,y}$ are detailed in Appendix A1

$$\begin{aligned} &\frac{\partial}{\partial x}\left(\frac{\rho \cdot h^3}{12 \cdot \eta \cdot \|\mathbf{v}_e\|}\frac{\partial p}{\partial x}\right) + \frac{\partial}{\partial y}\left(\frac{\rho \cdot h^3}{12 \cdot \eta \cdot \|\vec{\mathbf{v}}_e\|}\frac{\partial p}{\partial y}\right) \\ &\approx \frac{1}{\Delta x^2}\left[\varepsilon^x_{i-\frac{1}{2},j} \cdot p_{i-1,j} - \left(\varepsilon^x_{i-\frac{1}{2},j} + \varepsilon^x_{i+\frac{1}{2},j}\right)p_{i,j} + \varepsilon^x_{i+\frac{1}{2},j} \cdot p_{i+1,j}\right] \\ &+ \frac{1}{\Delta x^2}\left[\varepsilon^y_{i,j-\frac{1}{2}} \cdot p_{i,j-1} - \left(\varepsilon^y_{i,j-\frac{1}{2}} + \varepsilon^y_{i,j+\frac{1}{2}}\right)p_{i,j} + \varepsilon^y_{i,j+\frac{1}{2}} \cdot p_{i,j+1}\right] \end{aligned} \tag{10}$$

$$\begin{aligned} &\cos(\varphi_e)\frac{\partial(\rho \cdot h)}{\partial x} + \sin(\varphi_e)\frac{\partial(\rho \cdot h)}{\partial y} \approx \frac{1}{\Delta x} \\ &\cdot [\cos(\varphi_e) \cdot (\rho_{i,j} \cdot h_{i,j} - \rho_{i-1,j} \cdot h_{i-1,j}) + \sin(\varphi_e) \\ &\cdot (\rho_{i,j} \cdot h_{i,j} - \rho_{i,j-1} \cdot h_{i,j-1})] \end{aligned} \tag{11}$$

As indicated by Wang et al. [7], following the discretization of the Poiseuille and Couette flow terms, a system of linear equations with unknown pressures is obtained. By assuming $p_{i,j}$, $p_{i+1,j}$, and $p_{i-1,j}$ as the unknown variables and moving the terms related to $p_{i,j-1}$ and $p_{i,j+1}$ to the right-hand side, the discrete Reynolds equation can be solved. The form of the linear equation set is presented in Eq. (12) for the iteration index (s) [7]

$$A^{(s)}_{i,j} \cdot p^{(s+1)}_{i-1,j} + B^{(s)}_{i,j} \cdot p^{(s+1)}_{i,j} + C^{(s)}_{i,j} \cdot p^{(s+1)}_{i+1,j} = \delta^{(s)}_{i,j} \tag{12}$$

Typically, just the Poiseuille flow terms are used to build the coefficient matrix in Eq. (12), which might affect the numerical stability, for example, in ultrathin lubricant films. The semi-system approach overcomes this problem by building the coefficient matrix in Eq. (12) by considering both Poiseuille and Couette flow components. In this case, the elastic displacement (u_z) is used as a function of the unknown pressures in order to calculate the Couette flow terms [7]. The numeric calculation of the elastic displacement presented in Eq. (3) is made by Eq. (13), where the summation replaced the double integral. A critical factor in this numerical solution is the Coefficient of Influence Matrix ($D^{i,j}_{k,l}$), which evaluates how an elemental pressure, $p_{k,l}$, affects the numeric displacement at a response point, $(u_z)_{i,j}$ [16]

$$(U_z)_{i,j} = \frac{1}{\pi \cdot E^*} \cdot \sum_{k=1}^{N_x}\sum_{l=1}^{N_y} \mathbf{D}^{\mathbf{i,j}}_{\mathbf{k,l}} \cdot \mathbf{p}_{\mathbf{k,l}} \tag{13}$$

The Coefficient of Influence Matrix depends only on the geometric mesh structure, and its accuracy is also influenced by the piecewise interpolation function used for approximating the pressure distribution. According to Wang and Zhu [21], they do not depend on contact geometry, material properties, surface roughness, and operating conditions. The distance between the loading point (k, l) and the response point (i, j) determines each coefficient, regardless of the specific locations of these two points. If a uniform grid is employed ($\Delta x = \Delta y$), the distance can be evaluated by $|i-k|$ and $|j-l|$. With the zero-order approximation, pressure is assumed to be constant in each rectangular mesh element, so an analytical solution of Eq. (3) can be found [21]. Appendix A2 presents the Coefficient of Influence Matrix calculation.

Therefore, Eq. (13) can also be represented as a multiple diagonal matrix of the unknown pressures, $p_{i,j}$, $p_{i+1,j}$, and $p_{i-1,j}$, which can then be added to Eq. (12) to implement the semi-system method [7,21]. There are different forms of implementing the semi-system method. Wang et al. [7] presented six different approaches. Their work provides all the detailed expressions for these other implementations. However, here one presents only the computational implementation that best suits the experimental results. Equations (C1)–(C4), in Appendix A3, present the coefficient matrixes for Eq. (12) [7].

3 Thermal Elastohydrodynamic Lubrication Model

In order to implement a TEHL model, one must evaluate the sliding friction and temperature rise inside the contact area. Consequently, it is necessary to consider friction and flash temperature together [11]. The mixed lubrication friction is assumed to be a combination of the hydrodynamic friction at the lubricant locations and boundary friction at the asperity contacts. A TEHL model will use a succession of EHL iterations for different temperature fields until convergence is achieved [10].

Using Bair and Winer's non-Newtonian viscous-elastic fluid model [22], one can calculate the shear stress (τ) in the lubricant film (hydrodynamic areas) [13], as presented in Eq. (14)

$$\dot{\gamma} = \frac{\dot{\tau}}{G_\infty} - \frac{\tau_L}{\eta} \cdot \ln\left(1 - \frac{\tau}{\tau_L}\right) \tag{14}$$

The lubricant limiting yield shear stress (τ_L) and the lubricant limiting elastic shear modulus (G_∞) are functions of pressure and temperature. Bair and Winer [22] suggested a linear relation, as indicated in Eqs. (15) and (16). Preferably, the constants α_τ, β_τ, α_G, and β_G should be obtained experimentally [22]. In alternative, one can adjust these values based on the coefficient of friction measurements using an optimization algorithm [23]. Nevertheless, some caution should be exercised when using these values. Please notice that τ_L and G_∞ can be written in several different forms, as discussed by He et al. [13]. Keep in mind that each one will impact the friction and temperature rise in different forms. This particular study uses the linear approach for its simplicity.

$$\tau_L = (\alpha_\tau + \beta_\tau \cdot T) \cdot p \tag{15}$$

$$G_\infty = (\alpha_G + \beta_G \cdot T) \cdot p \tag{16}$$

Assuming the approximation for lubricant shear strain rate ($\dot{\gamma}$) presented in Eq. (17) [13], and using the same discretization utilized for the EHL model, one obtains Eq. (18), which can be solved iteratively at each node of the computational mesh to determine the film's shear stress distribution. The Bisection Method was employed in this study, with shear stresses ranging from zero to $0.9999\tau_{Li,j}$. The solution is assumed to be equal to $\tau_{Li,j}$ if the Bisection Method fails to find one when the trial shear stress exceeds $0.9999\tau_{Li,j}$ [22]

$$\dot{\gamma} = \frac{\|\mathbf{v}_e\| \cdot \text{SRR}}{h} \tag{17}$$

$$\frac{\tau_{i,j}-\tau_{i-1,j}}{\Delta x}-\frac{\tau_L i,j \cdot G_\infty i,j}{\eta_{i,j}\cdot\|\mathbf{v}_e\|}\cdot\ln\left(1-\frac{\tau_{i,j}}{\tau_L i,j}\right)-\frac{\mathrm{SRR}\cdot G_\infty i,j}{h_{i,j}}=0 \tag{18}$$

The shear stress at the asperity contacts is assumed to be directly proportional to the local pressure and is obtained through the coefficient of boundary friction (μ_b), as shown in Eq. (19). Usually, μ_b varies between 0.07 and 0.15, can be determined experimentally, and is adopted as a constant [13]

$$\tau_{i,j}=\mu_b\cdot p_{i,j} \tag{19}$$

The total friction may be calculated by combining shear stresses over the whole domain, including the hydrodynamic and asperity contact regions. Nevertheless, surface temperature and friction are directly correlated since temperature affects lubricant properties, which will impact heat generation due to friction. As indicated in the present work, the surface temperature calculation is based on the theory of a moving heat source over a semi-infinite solid. In this case, the convection heat flow perpendicular to the velocity of the heat source is neglected. Also, the heat generated at the interface will be carried away by the two moving solid bodies through conduction. Under these assumptions, the surface temperatures are obtained by solving Eqs. (20) and (21) [11,13]

$$T_1=T_{b_1}+\left(\frac{1}{\pi\cdot\rho_1\cdot C_1\cdot\|\mathbf{v}_1\|\cdot k_1}\right)^{0.5}\cdot\int_{-x}^{\Theta}\frac{\frac{k_f}{h}\cdot[T_2(\chi)-T_1(\chi)]+\frac{q(\chi)}{2}}{(\Theta-\chi)^{0.5}}\,d\chi \tag{20}$$

$$T_2=T_{b_2}+\left(\frac{1}{\pi\cdot\rho_2\cdot C_2\cdot\|\mathbf{v}_2\|\cdot\cos(\theta)\cdot k_2}\right)^{0.5}\cdot\int_{-x}^{\Theta}\frac{\frac{k_f}{h}\cdot[T_1(\chi)-T_2(\chi)]+\frac{q(\chi)}{2}}{(\Theta-\chi)^{0.5}}\,d\chi \tag{21}$$

It should be noted that q, Eq. (22), is the heat produced by either friction in the asperity contact regions or viscous shear in the hydrodynamic areas. [13]

$$\mathbf{q}\cong\boldsymbol{\tau}\cdot\|\mathbf{v}_e\|\cdot\mathrm{SRR} \tag{22}$$

Calculating T_1 and T_2 requires a division of the solution domain into many differential strips parallel to $\mathbf{v}_1$ and $\mathbf{v}_2$, respectively. The computational discretization follows the same one used for the EHL calculation. In this sense, one can apply Eqs. (18) and (19) along each differential strip in order to obtain a temperature field. The mathematical development is presented in detail by Wang and Zhu [21]. The discretized equations used in this study are shown in Eqs. (23) and (24). The convenient notation G_1, G_2, I_1, I_2, J_1 and J_2 are detailed in Appendix A4

$$T_1 i+1,j=\frac{I_1\cdot(1+J_2)+I_2\cdot J_1+G_2\cdot J_1\cdot q_{i+1}+G_1\cdot q_{i+1}\cdot(1+J_2)}{1+J_1+J_2} \tag{23}$$

$$T_2 i+1,j=\frac{I_2\cdot(1+J_1)+I_1\cdot J_2+G_1\cdot J_2\cdot q_{i+1}+G_2\cdot q_{i+1}\cdot(1+J_1)}{1+J_1+J_2} \tag{24}$$

Note that the nodal temperatures $T_{1i+1,j}$ and $T_{2i+1,j}$ are evaluated step by step based on the boundary conditions of $T_{10},j=T_{b_1}$ and $T_{20},j=T_{b_2}$. When calculating $T_{1i+1,j}$ and $T_{2i+1,j}$ the constants $T_{1i,j}$, $T_{2i,j}$, G_1, G_2, I_1, I_2, J_1, and J_2 are known. Therefore, the surface temperature along each differential strip can be computed, and the temperature distributions over the entire domain can be obtained [21]. Once one obtains the surface temperatures and assumes only thermal conductivity across the lubricant film, it is possible to determine a temperature distribution along the film thickness ($T_{fi,j,m}$), as indicated in Eq. (25). Also, the coordinate m represents a fraction of film thickness at node i,j in the z coordinate. For instance, this work divided the film thickness z coordinate into five nodes. Therefore, m is equal to 0.25, 0.50, and 0.75 in Eq. (25). Since $m=0$ represents $T_{1i,j}$ and $m=1$ represents $T_{2i,j}$, there is no need for a new calculation

$$T_f\, i,j,m=\frac{\tau_{i,j}\cdot\|\mathbf{v}_e\|\cdot\mathrm{SRR}\cdot h_{i,j}}{2\cdot k_f\, i,j}\cdot(m-m^2)+T_1 i,j\cdot(1-m)+T_2 i,j\cdot m \tag{25}$$

Now that the temperature fields are available, it is necessary to update the lubricant properties, ρ, η, α_{Gold}, k_f, τ_L, and G_∞ in an iterative procedure, as indicated by Wang et al. [10]. In this study, these values are modified node by node using an average temperature field ($T_{avgi,j}$) obtained from the five nodes in the z coordinate, as indicated in Eq. (26)

$$T_{avgi,j}=\frac{T_{1i,j}+T_{f\,i,j,m=0.25}+T_{f\,i,j,m=0.50}+T_{f\,i,j,m=0.75}+T_{2i,j}}{5} \tag{26}$$

After the problem is iteratively solved, one can use the pressure distribution and shear stress distribution over the contact area to obtain a coefficient of friction distribution, as shown in Eq. (27) and to estimate a global value for the coefficient of friction by considering the total shear force and the total normal force, as in Eq. (28). Please note that one can apply the same approach in the EHL (or PEHL) to calculate the coefficient of friction distribution using a constant temperature field

$$\mu_{i,j}=\left.\frac{\tau_{i,j}}{p_{i,j}}\right|_A \tag{27}$$

$$\mathrm{CoF}=\frac{\sum_{i=1}^{N_x}\sum_{j=1}^{N_y}(\boldsymbol{\tau}\cdot\Delta x^2)}{\sum_{i=1}^{N_x}\sum_{j=1}^{N_y}(\mathbf{p}\cdot\Delta x^2)} \tag{28}$$

As previously mentioned, based on the coefficient of friction value presented in Eq. (28), one can adjust the constants α_τ, β_τ, α_G, and β_G. The basic idea is managing to find four constants that produce a specific value of CoF, usually gathered from experimental evaluation. The numeric procedure consists of using a minimization algorithm to evaluate the difference between the experimental CoF and the CoF obtained from the simulation in full film lubrication. This study uses the Nelder–Mead method to minimize the CoF error, as indicated in Eq. (29), by changing the constants α_τ, β_τ, α_G, and β_G

$$\mathrm{Error}_{\mathrm{CoF}}=|\mathrm{CoF}-\mathrm{CoF}_{\mathrm{exp}}| \tag{29}$$

4 Plasto-Elastohydrodynamic Lubrication Model

In the PEHL model proposed by Azam et al. [12], constitutive changes are made in the EHL model solver to obtain the pressure distribution and film thickness. In this approach, a pressure limit is set for each node based on the material yield strength (σ_{yield}) or hardness. By truncating the pressure field, the load balance is directly affected, leading to an increase in the number of points required for the equilibrium. This particular approach was chosen for its simplicity and good agreement with other solutions, as presented by the author.

The main modification is related to the load balance condition. Since the points that undergo yielding are limited to the yielding pressure, an auxiliary pressure matrix ($\hat{p}_{k,l}^{(s+1)}$) is created, where the pressure nodes that exceed p_{yield} are truncated to this limit value, as defined in Eq. (30), and then used to calculate the load balance indicated in Eq. (31)

$$\forall\hat{\mathbf{p}}_{\mathbf{k,l}}^{(\mathbf{s+1})}>p_{yield}\Rightarrow\hat{\mathbf{p}}_{\mathbf{k,l}}^{(\mathbf{s+1})}=p_{yield} \tag{30}$$

Table 1 Parameter inputs for contact validation

	Bodies' properties	
Parameter	Reference value [4]	Current study
Normal load (P)	–	38.50 N
Principal relative radii of curvature ($R_x = R_y$)	0.01270 m	0.01270 m
Equivalent Young's modulus (E^*)	58.5 GPa	58.5 GPa
Maximum Hertz pressure (p_h)	0.54 GPa	0.54 GPa
Contact radius (a)	0.184 mm	0.184 mm
Amplitude (Δ)	0.08 μm	0.08 μm
Wavelength (λ)	59 μm	59 μm
Entrainment velocity ($\lVert \mathbf{v}_e \rVert$)	–	0.0487 m/s
Slide-to-roll ratio (SRR)	–	1.0
Density of bodies ($\rho_1 = \rho_2$)	–	7850.0 kg/m^3
Specific heats of bodies ($C_1 = C_2$)	–	460.0 J/(kg $\cdot^\circ$ C)
Thermal conductivity of bodies ($k_1 = k_2$)	–	46.0 W/(m $\cdot^\circ$ C)
Yield strength (σ_{yield})	–	300 MPa
Yielding pressure (p_{yield})	–	690 MPa

	Lubricant's properties	
Parameter	Reference value	Current study
Dynamic viscosity (η_T)@33.3°C	1.22 Pa · s	1.22 Pa · s
Dynamic viscosity (η_T)@0.0°C	–	13.01 Pa · s
Dynamic viscosity (η_T)@40.0°C	–	0.85 Pa · s
Dynamic viscosity (η_T)@100°C	–	0.08 Pa · s
Lubricant density (ρ_T)@15°C	–	860.0 kg/m^3
Oil thermal expansion coefficient (γ_T)	–	$5.5 \cdot 10^{-4}$ °C^{-1}
Temperature-viscosity coefficient (β)	–	0.057 °C^{-1}
Pressure-viscosity coefficient (α_{Gold})	22.5 GPa^{-1}	22.5 GPa^{-1}
s_G	–	7.3777
t_G	–	0.1534
Thermal conductivity of lubricant (k_f)@33.3°C	–	0.1402 W/(m $\cdot^\circ$ C)
Lubricant limiting yield shear stress constant (α_τ)	–	4.1
Lubricant limiting yield shear stress constant (β_τ)	–	$2.7 \cdot 10^{-2}$ °C^{-1}
Lubricant limiting elastic shear modulus constant (α_G)	–	$9.5 \cdot 10^{-2}$
Lubricant limiting elastic shear modulus constant (β_G)	–	$3.5 \cdot 10^{-4}$ °C^{-1}
Boundary coefficient of friction (μ_b)	–	0.10

	Other parameters	
Parameter	Reference value	Current study
Dimensionless material parameter (G^*)	2632	2633
Dimensionless speed parameter (U^*)	$4 \cdot 10^{-11}$	$4.00 \cdot 10^{-11}$
Dimensionless load parameter (W^*)	$2.08 \cdot 10^{-6}$	$2.04 \cdot 10^{-6}$
Mesh node number ($N_x = N_y$)	513	512
$\Delta x = \Delta y$	$0.374 \cdot 10^{-5}$m	$1.111 \cdot 10^{-5}$ m

$$W = \sum_{k=1}^{N_x} \sum_{l=1}^{N_y} \left(\hat{\mathbf{p}}_{\mathbf{k,l}}^{(\mathbf{s+1})} \cdot \Delta x^2\right) \tag{31}$$

However, one must keep in mind that the original pressure matrix still exists and it is used to compute solid displacement, that is, elastoplastic displacement $(u_z)_{i,j}^{ep}$. The final plastic deformation can be obtained by subtracting the elastoplastic displacement $(u_z)_{i,j}^{ep}$ from the elastic displacement $(u_z)_{i,j}^{e}$ that would result if the reduced pressure matrix were present in an equivalent elastic contact [12], given by Eq. (32)

$$(u_z)_{i,j}^{p} = (u_z)_{i,j}^{ep} - (u_z)_{i,j}^{e} = \frac{1}{\pi \cdot E^*} \cdot \sum_{k=1}^{N_x} \sum_{l=1}^{N_y} \left(\mathbf{D}_{\mathbf{k,l}}^{\mathbf{i,j}} \cdot \mathbf{p}_{\mathbf{k,l}}^{(\mathbf{s+1})}\right) - \frac{1}{\pi \cdot E^*} \cdot \sum_{k=1}^{N_x} \sum_{l=1}^{N_y} \left(\mathbf{D}_{\mathbf{k,l}}^{\mathbf{i,j}} \cdot \hat{\mathbf{p}}_{\mathbf{k,l}}^{(\mathbf{s+1})}\right) \tag{32}$$

5 Proposed Thermal Plasto-Elastohydrodynamic Lubrication Model

A thermal plasto-elastohydrodynamic lubrication (TPEHL) model combines in a single algorithm the thermal elastohydrodynamic lubrication (TEHL) model to update lubricant temperature due to friction effects and the plasto-elastohydrodynamic lubrication (PEHL) model, in order to restrict the pressure field. Appendix A5 shows the TPEHL algorithm implemented based on these assumptions, while Appendix A6 gives the PEHL model required in the TPEHL second step. It is important to remember that the presented result adapts in a single computational solution to the models developed by other authors [7,10–12] in isolated solutions. These particular solutions were chosen in this work due to their simplicity and

Table 2 Validation conditions

Condition	Entrainment velocity ($\lVert \boldsymbol{v}_{\mathbf{e}} \rVert$)	Maximum Hertz Pressure ($\mathbf{p_h}$)	Contact radius ($\mathbf{a}$)	Surface profile
Condition 1	0.0487 m/s	0.54 GPa	0.184 mm	Sinusoidal
Condition 2	1.0000 m/s	0.54 GPa	0.184 mm	Sinusoidal
Condition 3	0.0487 m/s	1.13 GPa	0.385 mm	Sinusoidal
Condition 4	1.0000 m/s	1.13 GPa	0.385 mm	Sinusoidal
Condition 5	1.0000 m/s	1.13 GPa	0.385 mm	Artificial roughness

minimal implementation changes in standard EHL models. On the other hand, the assumptions used by the TEHL and PEHL models are inherited by the TPEHL model and, therefore, may impact the results obtained.

In order to show the capabilities of the TPEHL implemented here, this section compares the results obtained with EHL, TEHL, PEHL, and TPEHL models for five distinct conditions, summarized in Table 2

- Condition (1): the classic results from Venner and Lubrecht [4] obtained with the parameters in Table 1.
- Condition (2): similar to Condition (1), but using a higher entrainment velocity (1.00 m/s). The other parameters remained the same.
- Condition (3): similar to Condition (1), but using a higher load (350.0 N). The other parameters remained the same;

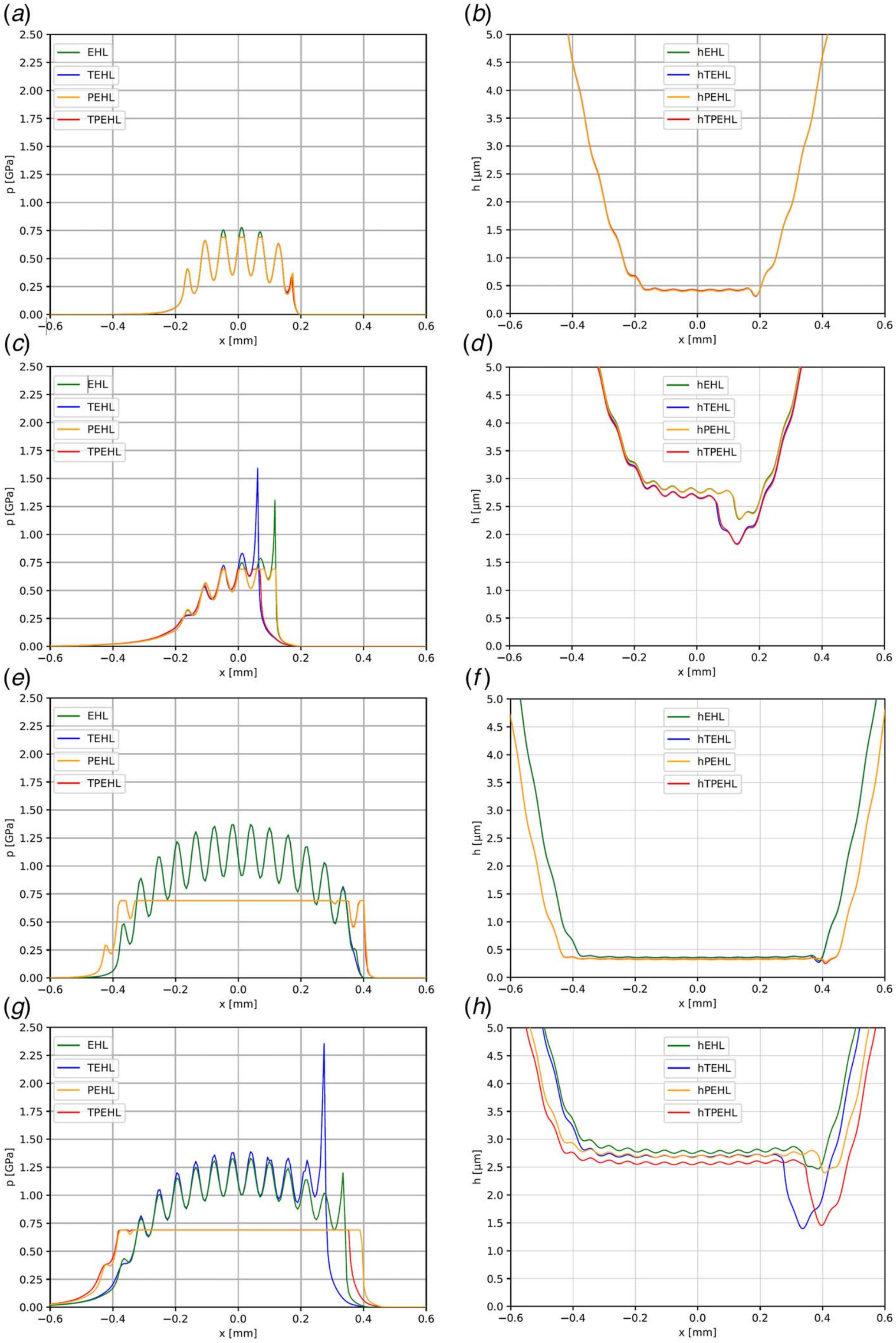

Fig. 2 **Pressure and film thickness simulations: (*a*) and (*b*) Condition 1; (*c*) and (*d*) Condition 2; (*e*) and (*f*) Condition 3; (*g*) and (*h*) Condition 4**

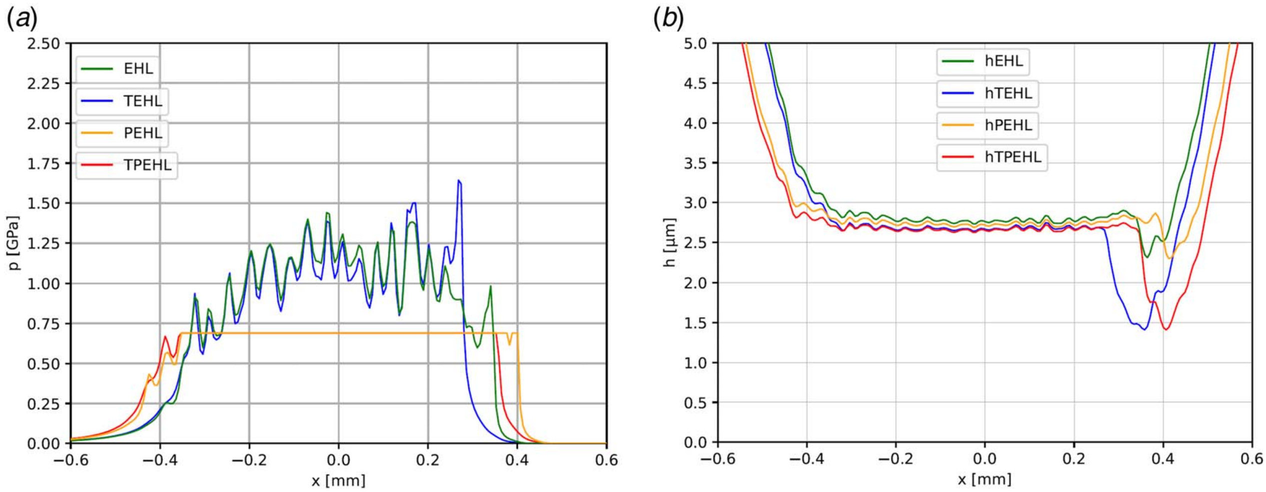

Fig. 3 (*a*) Pressure and (*b*) film thickness simulation for artificial roughness in Condition 5

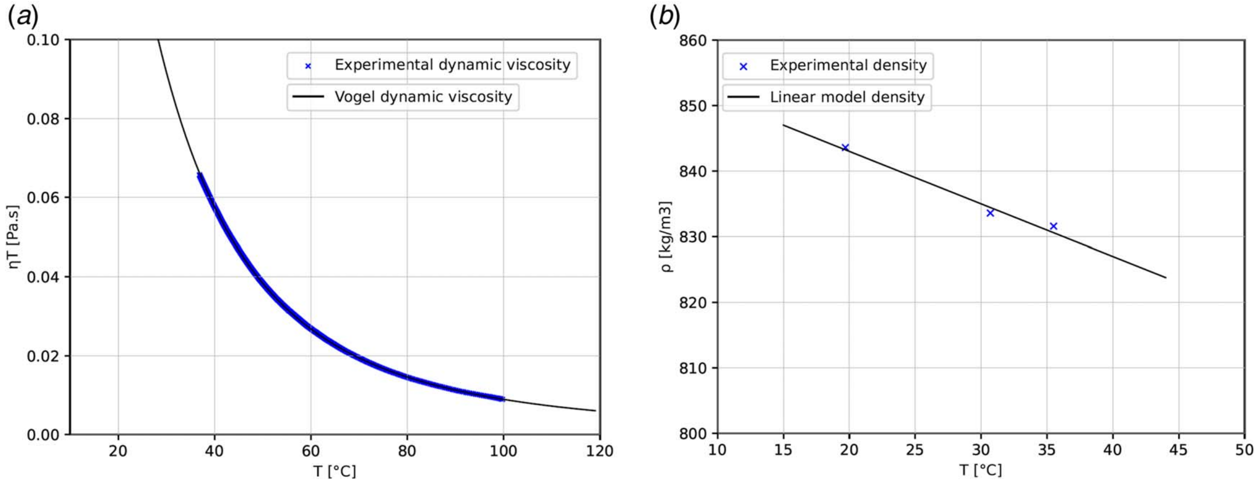

Fig. 4 ISO VG68 dynamic viscosity and density

Table 3 Experimental dynamic viscosity

Parameter	Value
Dynamic viscosity (η_T)@40.0°C	0.0576 Pa · s
Dynamic viscosity (η_T)@70.1°C	0.0194 Pa · s
Dynamic viscosity (η_T)@99.5°C	0.0090 Pa · s
Density (ρ_T)@19.7°C	843.6 kg/m^3
Density (ρ_T)@30.7°C	833.6 kg/m^3
Density (ρ_T)@35.5°C	831.6 kg/m^3

- Condition (4): similar to Condition (1), but using a higher entrainment velocity (1.00 m/s) and a higher load (350.0 N). The other parameters remained the same;
- Condition (5): similar to Condition (4), but using an artificial roughness. Notice that in this last analysis, the sinusoidal profile was substituted by a Gaussian distribution with a root-mean-square variance (S_q) equal to 0.08 μm. The other parameters remained the same.

Figure 2 compares the results obtained from the four discussed models (EHL, TEHL, PEHL, and TPEHL) for all the sinusoidal conditions, where it is possible to see the pressure distribution and the film thickness. Four points to highlight here are as follows:

- Since Condition 1 presents low entrainment velocity (0.04870 m/s) and low load (38.5 N), both thermal and plastic effects are minimal (or even neglectable). Therefore, the four discussed models (EHL, TEHL, PEHL, and TPEHL) presented very similar results in terms of pressure (Fig. 2(*a*)) and film thickness (Fig. 2(*b*)). The presented results are in clear concordance with the classic results from Venner and Lubrecht [4].
- Once the entrainment velocity increased (1.00 m/s) in Condition 2, but the load (38.5 N) remained, thermal effects started to be more prone, but plastic effects were still minimal. In this sense, one can notice a pressure spike in Fig. 2(*c*) for the TEHL model and a reduction in film thickness (Fig. 2(*d*)), namely at the contact exit, showing the modifications introduced by the thermal effect. These results are consistent with the TEHL models in the literature [1,9–11], and more importantly, there is an explicit agreement between the results obtained with the TEHL (blue) and TPEHL (red), as it should be since Condition 2 induces thermal effects but minimal plastic changes.
- Condition 3 presents another scenario where the entrainment velocity was kept low (0.04870 m/s) and the load increased (350.0 N). Therefore, thermal effects are minimized, but the plastic phenomenon becomes more significant. Given the yielding pressure (0.690 GPa) assumed to truncate the pressure field in the PEHL model, it is possible to see in Fig. 2(*e*) a flat pressure distribution over a broader contact area, also illustrated in Fig. 2(*f*) for the film thickness, which also presented a slight reduction. The same behavior is reported in the

Table 4 Parameter inputs for the coefficient of friction

Parameter	Value
Normal load (P)	50.0 N
Principal relative radii of curvature ($R_x = R_y$)	0.009525 m
Mesh node number ($N_x = N_y$)	299
Equivalent Young's modulus (E^*)	115.38 GPa
Maximum Hertz Pressure (p_h)	1.12 GPa
Contact radius (a)	0.146 mm
Disc average roughness (R_a)	0.30 μm
Ball average roughness (R_a)	0.02 μm
Dynamic viscosity (η_T)@40.0°C	0.0576 $\text{Pa} \cdot \text{s}$
Dynamic viscosity (η_T)@70.1°C	0.0194 $\text{Pa} \cdot \text{s}$
Dynamic viscosity (η_T)@99.5°C	0.0090 $\text{Pa} \cdot \text{s}$
Lubricant density (ρ_T)@25.0°C	827.0 kg/m^3
Oil thermal expansion coefficient (γ_T)	$9.7 \cdot 10^{-4}\ ^\circ\text{C}^{-1}$
Pressure-viscosity coefficient (α_{Gold})@25.0°C	14.3 GPa^{-1}
Thermal conductivity of lubricant (k_f)@25.0°C	0.14 $\text{W}/(\text{m} \cdot ^\circ \text{C})$
Lubricant limiting yield shear stress constant α_τ	4.41
Lubricant limiting yield shear stress constant β_τ	$2.97 \cdot 10^{-2}\ ^\circ\text{C}^{-1}$
Lubricant limiting elastic shear modulus constant α_G	$7.98 \cdot 10^{-2}$
Lubricant limiting elastic shear modulus constant β_G	$3.75 \cdot 10^{-4}\,^\circ\text{C}^{-1}$
Density of bodies 1 and 2 ($\rho_{1,2}$)	7850.0 kg/m3
Specific heats of bodies 1 and 2 ($C_{1,2}$)	460.0 $\text{J}/(\text{kg} \cdot ^\circ \text{C})$
Thermal conductivity of bodies 1 and 2 ($k_{1,2}$)	46.0 $\text{W}/(\text{m} \cdot ^\circ \text{C})$
Slide-to-roll ratio (SRR) #1	0.15
Slide-to-roll ratio (SRR) #2	0.50
Hardness (HV)	820 HV
Yielding pressure (p_{yield})	2.00 GPa

literature [8,12]. Note again that the TPEHL model predicted similar results to the PEHL since the thermal effects can be neglected in this condition.

- Condition 4 closes the sinusoidal analyses with both entrainment velocity (1.00 m/s) and load (350.0 N) higher than the original values used by Venner and Lubrecht [4]. Here, thermal and plastic effects take place. In this sense, in addition to the pressure field modifications (Fig. 2(*g*)), it is possible to note that the film thickness (Fig. 2(*h*)) predicted by the TPEHL model is smaller than the other film thicknesses using the isolated models. Clearly, in this situation, the combination of thermal and plastic effects generated a result that could not be predicted by an EHL, TEHL, or PEHL model alone.

For consistency, Fig. 3 presents the results for the artificial roughness used in Condition 5, where one can observe similar behavior to Condition 4.

From the analysis carried out in this section, it is worth highlighting the following:

- The TPEHL model implemented in this work had the capability to obtain the same results produced by the other models without the need for a preliminary evaluation. That is, under conditions in which only thermal effects, only plastic effects, or none of these were present, the results obtained by TPEHL were the same as TEHL, PEHL, or EHL;
- When present together, the combined effects of temperature and plasticity produced an effect different from what current isolated models predict. In fact, from the simulations, one

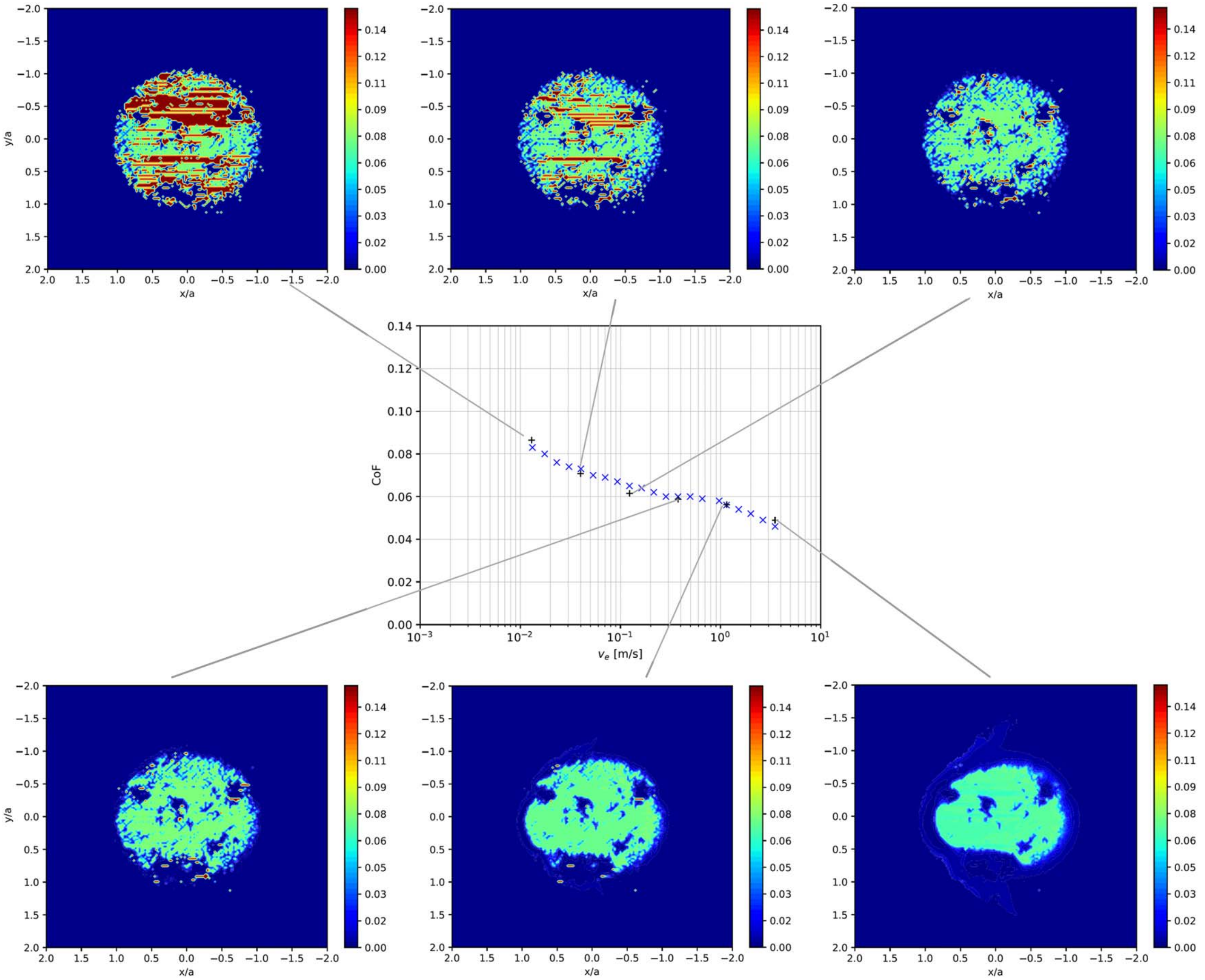

Fig. 5 Experimental CoF ("x") against simulated CoF ("+") for SRR 0.15 and CoF distribution maps

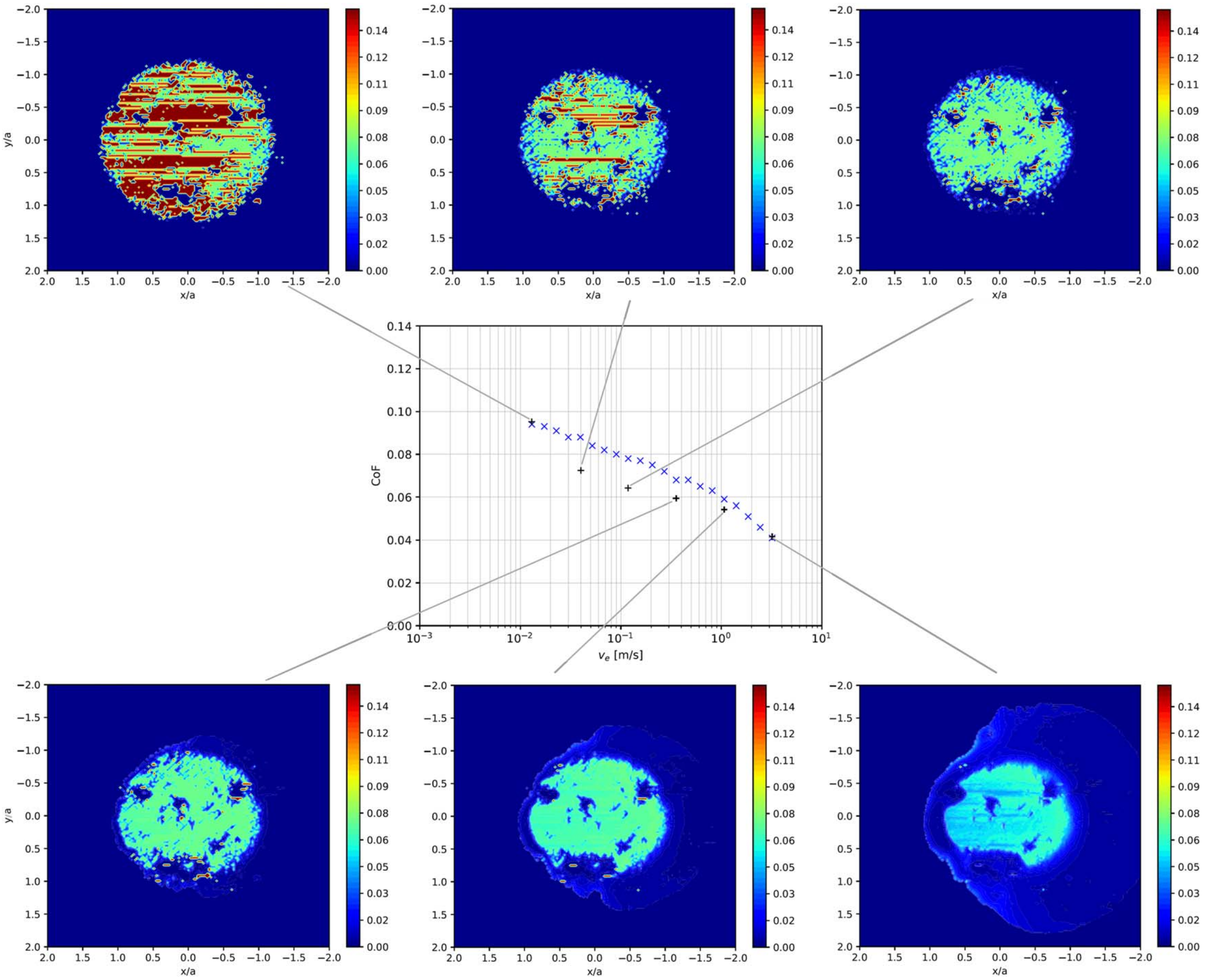

Fig. 6 Experimental CoF ("x") against simulated CoF ("+") for SRR 0.50 and CoF distribution maps

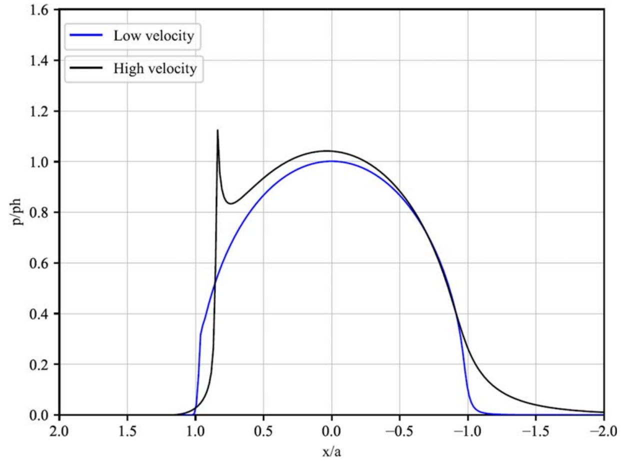

Fig. 7 Pressure distribution comparison for high and low entrainment velocities

can say that the expected film thickness decreases in the following order: EHL, TEHL/PEHL, and TPEHL.

6 Experimental Results and Numeric Validation

Motivated by the need for experimental validation, a set of predictions using the proposed TPEHL model were crossed against experimental results of coefficient of friction, film thickness, and rolling/sliding track width. Given the required lubricant properties in the TPEHL model, one chose a commercial ISO VG68 polyalphaolefin oil for this evaluation. This section details all experimental campaigns used to characterize the lubricant, as well as the results obtained from tests and simulations.

Table 5 Parameter inputs for film thickness (adapted from Ref. [24])

Parameter	Value
Normal load (P)	50.0 N
Equivalent Young's modulus (E^*)	147.28 GPa
Maximum Hertz pressure (p_h)	1.32 GPa
Contact radius (a)	0.135 mm
Disc average roughness (R_a)	0.00 (smooth)
Ball average roughness (R_a)	0.02 μm
Density of body 1 (ρ_1)—Sapphire	4000.0 kg/m^3
Density of body 2 (ρ_2)—Steel	7850.0 kg/m^3
Specific heat of body 1 (C_1)—Sapphire	750.0 J/(kg ·°C)
Specific heat of body 2 (C_2)—Steel	460.0 J/(kg ·°C)
Thermal conductivity of body 1 (k_1)—Sapphire	40.0 W/(m ·°C)
Thermal conductivity of body 2 (k_2)—Steel	46.0 W/(m ·°C)
Slide-to-roll ratio (SRR)#1	0.00
Slide-to-roll ratio (SRR)#2	1.00

6.1 Lubricant Dynamic Viscosity and Density. As indicated, one must know lubricant dynamic viscosity behavior as an input in

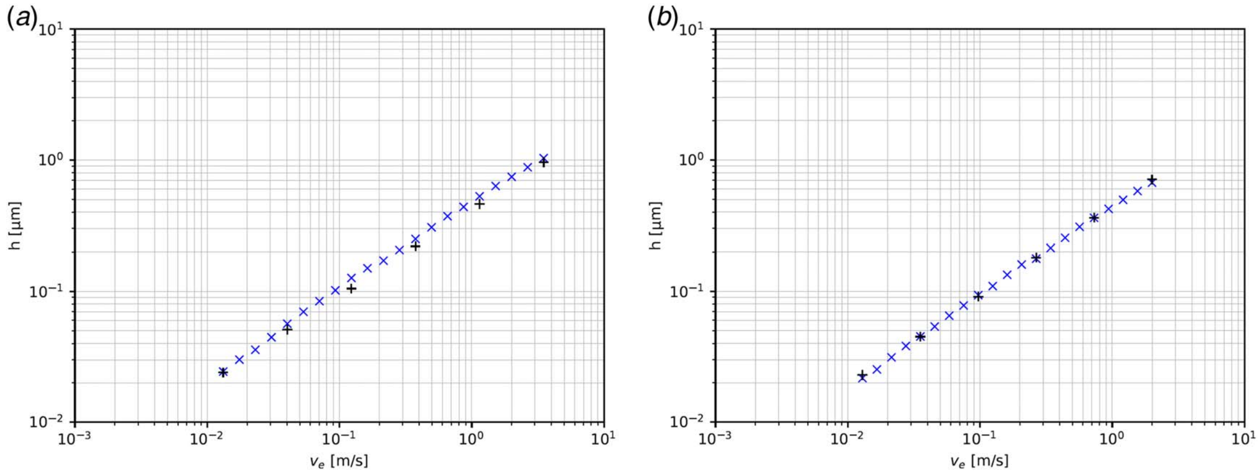

Fig. 8 Experimental film thickness ("+") against simulated film thickness ("+") for (*a*) SRR 0.00 and (*b*) 1.00

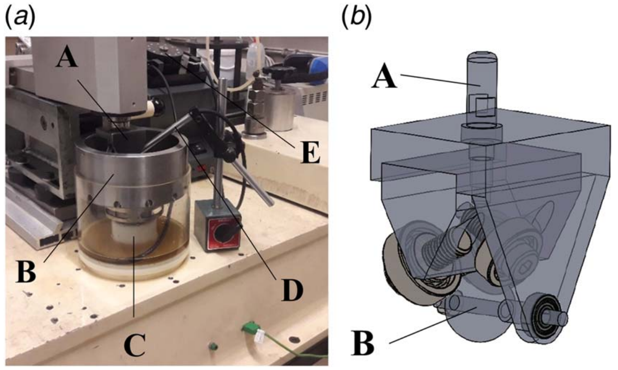

Fig. 9 (*a*) Ball-on-Disc system implemented and (*b*) support for the ball

the simulations. Equation (8) presents the used Vogel dynamic viscosity variation with the temperature. In that case, one has a triparametric (ξ, ζ and ψ) relation, which requires three distinct viscosity measurements. This property was measured using a vibro viscometer (SV-10 AND, Japan, 2008), between 99.76 °C and 36.86 °C. The experimental results are plotted in Fig. 4(*a*). The Vogel dynamic viscosity variation with the temperature is also shown in black. In that case, the required three parameters, ξ, ζ and ψ, were calculated using the experimental points shown in Table 3. The obtained values were $\xi = 8.390 \cdot 10^{-5}\ \mathrm{Pa \cdot s}$, $\zeta = 982.010\ {}^\circ\mathrm{C}$, and $\psi = 110.358\ {}^\circ\mathrm{C}$. It is possible to see a good agreement between experimental and calculated values.

The lubricant density at a given temperature (ρ_T) is a function that correlates the lubricant density at a reference temperature (ρ_0) with a specified temperature on the contact, as shown in Eq. (6). This is another essential parameter required for the simulations. Therefore, the lubricant density was measured using a portable density meter (Anton Paar, Austria). Table 3 presents the experimental data, while Fig. 4(*b*) shows the results plotted in blue. Using the Least Squares Method, one determined the oil thermal expansion coefficient (γ_T) as $9.7 \cdot 10^{-4}\ {}^\circ\mathrm{C}^{-1}$. The density curve is plotted in black. A correlation of 0.979 was obtained between the curve and experimental points.

6.2 Stribeck Curves. The first test for the proposed TPEHL model was to predict the Coefficient of Friction under different operational conditions. In this sense, Stribeck curve tests [13,14] were performed using an EHD2 Ball-on-Disc apparatus (PCS

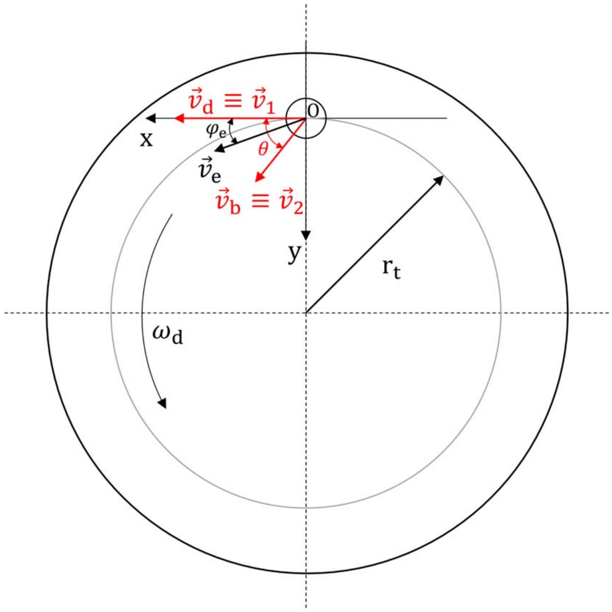

Fig. 10 Ball-on-disc kinematics scheme. Adapted from Ref. [25].

Instruments, England, 2014). Both ball and disc are made of 100Cr6 steel with a measured hardness of about 820 HV, which allows one to determine the yielding pressure for the simulations. Two different SRRs were applied in this campaign, 0.15 and 0.50, at room temperature. For each test, the entrainment velocity ($\|\mathbf{v}_e\|$) was in the range between 0.01 m/s and 3.50 m/s, with five repetitions. Table 4 presents in detail all parameters used for the test and simulations. The roughness used in the simulations was acquired using 3D Optical Profilometer equipment (Bruker NPFLEX™, Germany) and used without the application of filters; that is, roughness and waviness were present in the simulation.

Figure 5 shows the experimental CoF in "x" markers and the simulated results in "+" markers for the SRR 0.15. Similarly, Fig. 6 gives the experimental CoF in "x" markers and the simulated results in "+" markers for the SRR equal to 0.50. The boundary friction coefficient (μ_b) was assumed to be 0.14 in the simulations, given that the Stribeck curve did not achieve the boundary regime in order to obtain the actual value. Nevertheless, from an optimization point of view, one can also consider the boundary value as

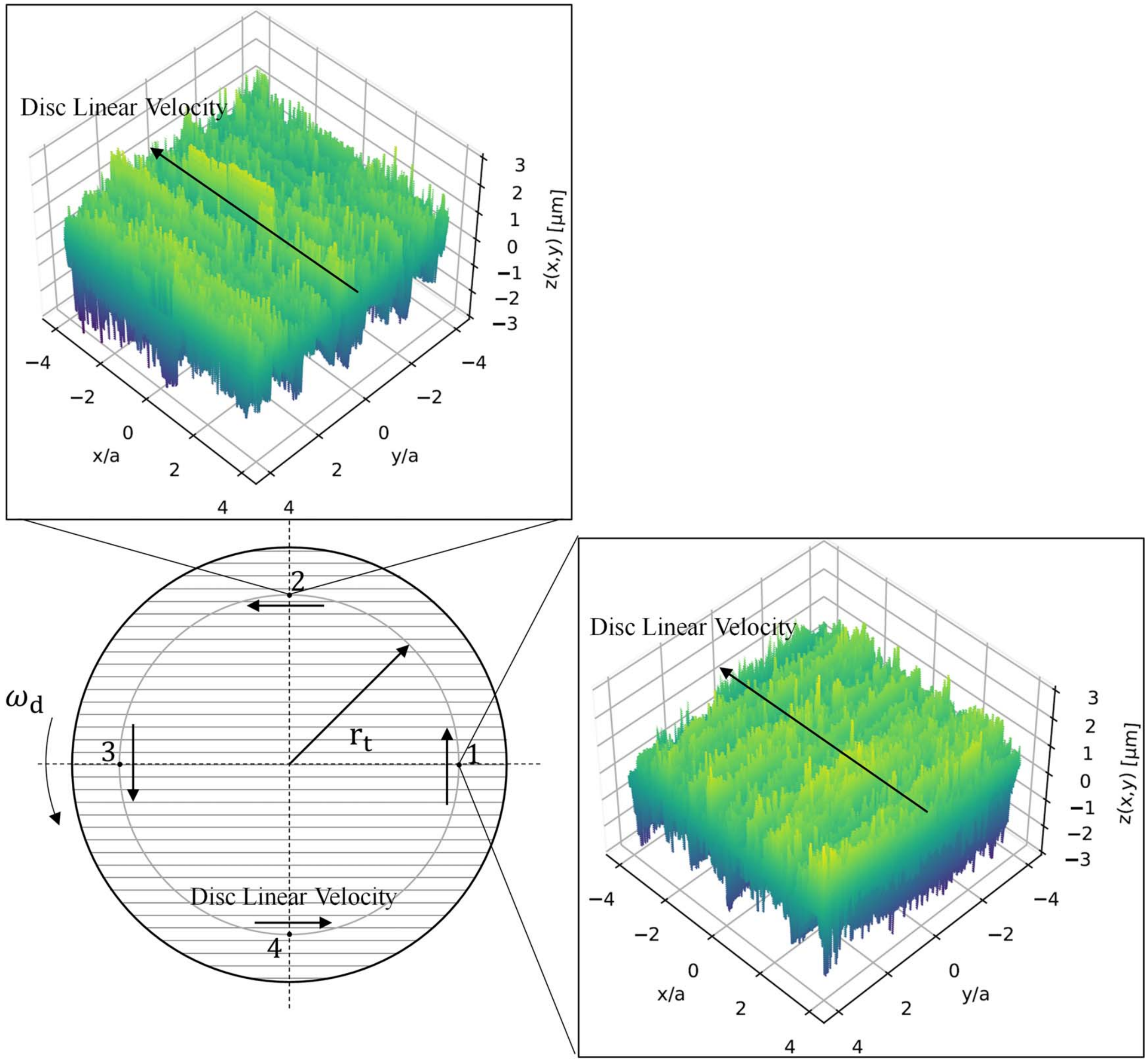

Fig. 11 Sample disc illustration for rolling contact assessment. Transversal roughness points 1 and 3. Longitudinal roughness points 2 and 4.

Table 6 Parameter inputs for the track width test and validation

Parameter	Value
Normal load (P)	50.0 N
Principal relative radii of curvature ($R_x = R_y$)	0.009525 m
Mesh node number ($N_x = N_y$)	597
Equivalent Young's modulus (E^*)	115.38 GPa
Maximum Hertz pressure (p_h)	1.12 GPa
Contact radius (a)	0.146 mm
Disc average roughness (R_a)	0.60 μm
Ball average roughness (R_a)	0.02 μm
Slide-to-roll ratio (SRR)#1	0.15
Slide-to-roll ratio (SRR)#2	0.30
Hardness (HV)	300 HV
Yielding pressure (p_{yield})	0.986 GPa

another constant to be adjusted. Figures 5 and 6 also present the CoF distribution obtained for the different conditions, where one can see the coefficient of boundary friction indicated in red ($\mu_{\mathrm{b}} = 0.14$). It is essential to highlight that the lubricant limiting yield shear stress (τ_L) and the lubricant limiting elastic shear modulus (G_∞) models have a significant impact on CoF prediction, as well explained by He et al. [13]. In this sense, the four constants (α_τ, β_τ, α_{G}, and β_{G}) used in Bair and Winer [22] linear relation had to be calibrated in this work using the experimental CoF value in the full film regime, similar to Brandão et al. [23]. The Nelder–Mead method to minimize the CoF error in Eq. (29) provided the values in Table 4.

A few aspects of CoF results deserve some discussion. First, as one can see both in Figs. 5 and 6, for the higher speeds, the CoF distribution presents a slight increase right in front of the contact entrance. This phenomenon is related to the gradual increase in pressure up to the contact inlet, which induces lubricant shear and, therefore, some friction. In other words, the friction in the lubricant starts with the pressure increase just before the contact inlet. On the other hand, this pressure increase at the entrance is less pronounced for the lower entrainment velocities, so the CoF increase right at the contact entry is less visible in the CoF maps distributions. The effect on the pressure distribution is illustrated in Fig. 7, where the highest and lowest velocities of the Stribeck curves were considered.

A second point to highlight is that the current TPEHL model presented a really good agreement for the SRR 0.15, while the SRR 0.50 condition showed some deviations for intermediate speeds.

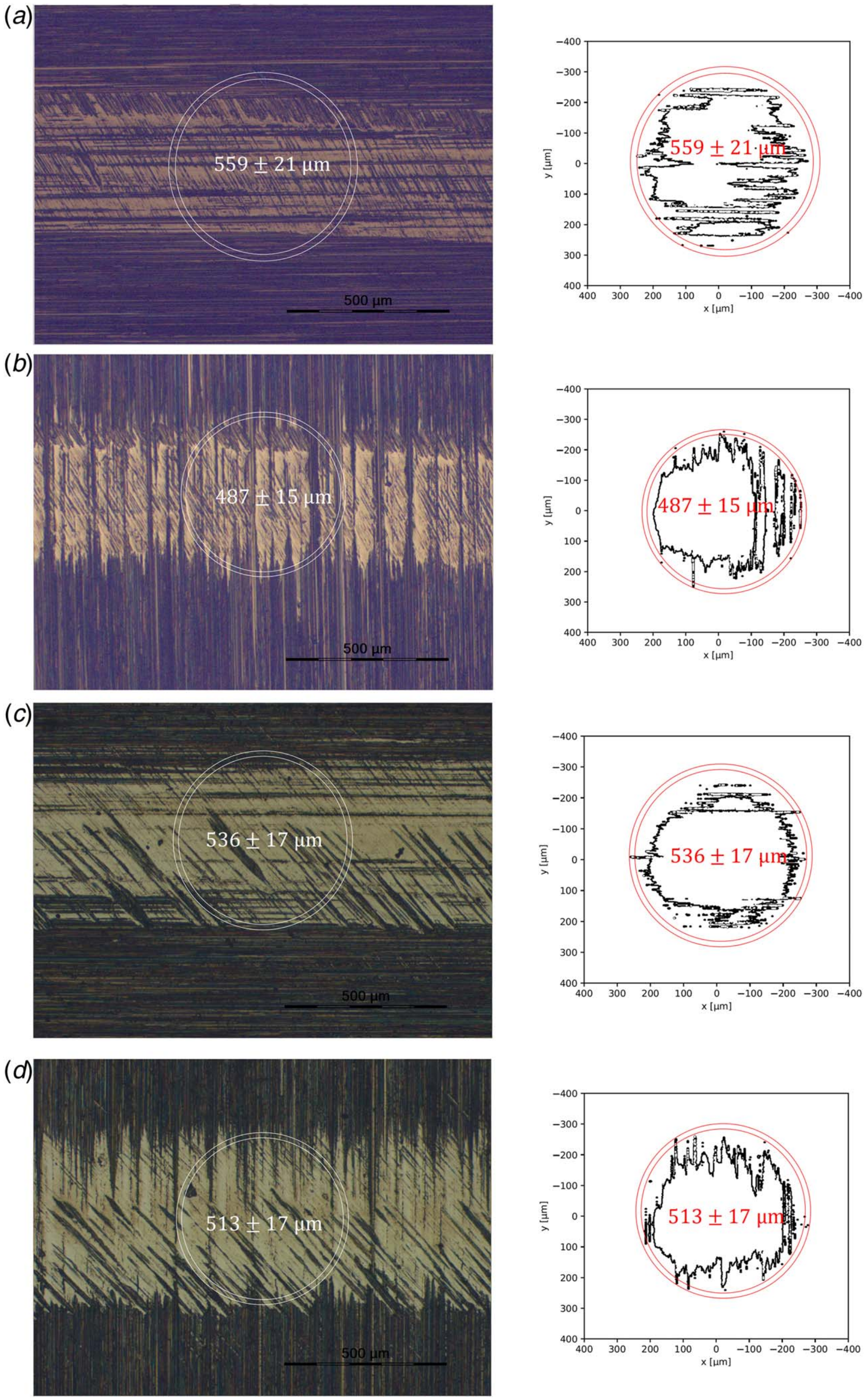

Fig. 12 Track width experimental and simulated result comparison: (*a*) longitudinal roughness for SRR 0.15, (*b*) transversal roughness for SRR 0.15, (c) longitudinal roughness for SRR 0.30, and (*d*) transversal roughness for SRR 0.30

These differences between model prediction and experimental value might be related to different factors, for instance, the thermal and plastic assumptions already discussed. However, the limitation of the proposed TPEHL model in considering a possible wear process could also explain the deviations and should be added to this list. Since at SRR 0.50 this wear process tends to be more significant, this may affect the CoF prediction in the current TPEHL model.

6.3 Film Thickness.

The EHD2 Ball-on-Disc apparatus (PCS Instruments, England, 2014) was also used for the film thickness tests. In that case, the ball is made of 100Cr6 steel, while a sapphire disc was employed to perform optical interferometry measurement. Two different SRRs were applied in this campaign, 0.00 and 1.00. For each test, the entrainment velocity ($\|\mathbf{v}_e\|$) was in the range between 0.01 m/s and 3.50 m/s. Table 5 presents all parameters used for the test and correlated simulations (complements in Table 4).

Figure 8 shows the experimental film thickness in blue and the simulated results in black for the SRR equal to 0.00 and 1.00. One can see good agreement between the experimental values and the TPEHL predictions. In this particular case, plastic effects are not expected, although thermal behavior will be present at least for SRR 1.00. In any case, prior evaluation is unnecessary, given that the model presented can deal with these situations autonomously.

6.4 Rolling/Sliding Contact Assessment. In order to perform rolling/sliding contact tests, it was necessary to adapt a Pin-on-Disc machine (Cameron Plint Tribology, England) to carry out Ball-on-Disc tests. Figure 9(*a*) shows the experimental system implemented: point A indicates the ball support, point B the lubricating oil collection system, point C the lubricating oil reservoir, point D the lubricating oil injection support, and point E the peristaltic pump for oil recirculating. Figure 9(*b*) presents the support in detail. The system uses the same 100Cr6 steel ball used for the Stribeck curve and film thickness tests. In addition, it allows static loads up to 300 N and Slide-to-Roll Ratios (SRRs) from 0.0 to 2.0.

The SRR control is obtained by rotating the support around the pin indicated by A in Fig. 9(*b*). Since the ball's movement is limited by the central axis, as shown by B in Fig. 9(*b*), the support rotation introduces different sliding/rolling levels on the contact. This support is based on the study developed by Gama et al. [25]. In their work, the authors analyze the contact kinematics and show that the entrainment velocity, presented in Eq. (33), entrainment velocity angle, shown in Eq. (34), and SRR, given by Eq. (35), are a function of the ball's axis angle (θ), as illustrated in Fig. 10

$$\|\mathbf{v}_e\| = r_t \cdot \omega_d \cdot \frac{\sqrt{1 + 3 \cdot \cos^2(\theta)}}{2} \tag{33}$$

$$\varphi_e = \tan^{-1}\left[\frac{\cos(\theta) \cdot \sin(\theta)}{1 + \cos^2(\theta)}\right] \tag{34}$$

$$\mathrm{SRR} = \frac{2 \cdot \sin(\theta)}{\sqrt{1 + 3 \cdot \cos^2(\theta)}} \tag{35}$$

The tested discs are made of 42CrMo4 steel, provided by the manufacturer with a 300 HV hardness. These samples present a grinding direction, as illustrated in Fig. 11. Therefore, the track width is affected by the relative position between the rolling and roughness directions. In this sense, it is necessary to distinguish transversal roughness (points 1 and 3) and longitudinal roughness (points 2 and 4). The roughness used in the simulations was acquired using 3D Optical Profilometer equipment (Bruker NPFLEX$^{\mathrm{TM}}$, Germany) and used without the application of filters. Table 6 summarizes the experimental parameters (complements in Table 4).

Figure 12 compares the experimental track width after 20 h of rolling contact test (about 500,000 cycles) and the estimated value using the current TPEHL model. In that case, the evaluation used the following criteria, the red outer circle contains 100% of the simulated contact points and accounts for the diameter upper limit, while the red inner circle represents 90% of the contact points and refers to the low diameter limit. This evaluation aimed to capture the variability observed in the track width. Considering the proper scale, the same circles were plotted in white on the experimental tracks in order to compare the predictions with the microscope images. Beyond the absolute values, one can see a good similarity between the circles and track width. It is safe to say that the TPEHL model predicted better track width values than Hertz theory (2a = 291 μm). It is also clear that the qualitative behavior is very similar concerning contact points and contact area distribution.

It is important to highlight that the choice for the 500,000 cycles test relies on the running-in concept, where the plastic deformation of rough peaks is dominant, but the wear process is still incipient. There is no doubt that wear mechanisms are involved in this contact, quite evident in the visible angle scars on the track. Therefore, since the presented TPEHL model does not deal with wear, it seems prudent to compare simulated results with the early stages of operation. Another essential point to underline concerns the hardening work on the surface, which is related to plastic deformation and is not considered in this model. A good way to numerically deal with this issue is to update surface hardness and roughness as input at each new simulation, which will allow following the track width development.

7 Conclusions

A good design should consider the effects of temperature and plastification in order to keep mechanical components' failure under control. However, understanding what happens inside the contact area for reliable operational predictions is complex. To contribute to this scenario, the current study presented a simplified thermal plasto-elastohydrodynamic lubrication (TPEHL) model for circular contact with real surface roughness capable of simulating the entire transition of lubrication regimes. The primary purpose of this work was to present to the reader a way to combine the effects of temperature and plastification in the circular contact, which up to now is little discussed in the technical literature. As a consequence of the validations presented for the different approaches, it was possible to compare the EHL, TEHL, PEHL, and TPEHL models under various operational conditions, showing that there are situations in which isolated TEHL and PEHL models may be insufficient and the TPEHL a viable solution.

Among the advantages of the presented model, one should mention the following:

- The minimal implementation changes in standard EHL models.
- There is no need for a preliminary assessment to verify whether thermal and plastic effects are negligible (or not) since these effects will naturally take place in the simulations.
- Despite the simplifications used in this study, it is essential to highlight that the proposed TPEHL model showed good agreement between the predictions and the experimental tests, particularly for the track width predictions.

Among the disadvantages of the presented approach, the following should be kept in mind:

- The simplifying assumptions used by the implemented TEHL and PEHL models, namely an infinitely large volume for the thermal equilibrium calculation and ideal plastic material behavior, are inherited by the TPEHL model and, therefore, may have an impact on the results obtained;
- Using a parameter optimization strategy for α_τ, β_τ, α_G, and β_G must be accompanied by caution as it can produce artificial results; and
- Wear mechanisms are not taken into account in the simulations, which may lead to deviations in CoF predictions, film thickness, and track width.

It is worth mentioning that this article is a starting point for integrated thermal and plastic models, and much more can be developed from here concerning the modeling assumptions and type of contacts. And finally, the presented results can be used to compare other approaches that integrate both effects.

Acknowledgment

The authors gratefully acknowledge the financial support of several projects and grants, namely, National Funds through Fundação para a Ciência e a Tecnologia (FCT) under the PhD Grant No. 2021.05562.BD; GEAR3D under project POCI-01-0247-FEDER-039848; LAETA under project UID/50022/2020.

Conflict of Interest

There are no conflicts of interest.

Data Availability Statement

The data sets generated and supporting the findings of this article are obtainable from the corresponding author upon reasonable request.

Nomenclature

a = Hertz contact radius (m)
m = fraction of film thickness in the z coordinate
q = heat generated over friction (W/m^2)
A = domain used to analyze the contact area
P = normal load applied to the contact (N)
T = temperature assumed for the lubricant (°C)
W = numerical load applied (N)
E^* = equivalent Young's modulus (Pa); $\left(\frac{1-\nu_1^2}{E_1}+\frac{1-\nu_2^2}{E_2}\right)^{-1}$
$h_{i,j}$ = film thickness at node i, j (m)
k_f = thermal conductivity of lubricant (W/(m·°C)), $\frac{0.12\cdot(1-1.667\cdot 10^{-4})\cdot T}{\rho_T}$
$k_{1,2}$ = thermal conductivity of bodies 1 and 2 (W/(m·°C))
$p_{i,j}$ = numerical pressure acting at node i, j (Pa)
$p_{k,l}$ = numerical pressure acting at node k, l (Pa)
r_t = sample disc track radius (m)
$\|\mathbf{v}_e\|$ = entrainment velocity (m/s), $\frac{|\mathbf{v}_2+\mathbf{v}_1|}{2}$
$\mathbf{v}_{1,2}$ = Velocity of bodies 1 and 2 (m/s)
$C_{1,2}$ = specific heats of bodies 1 and 2 (J/(kg·°C))
$E_{1,2}$ = Young's modulus of bodies 1 and 2 (Pa)
G_∞ = lubricant limiting elastic shear modulus (Pa)
$G_{1,2}$ = convenient notations to simplify Eqs. (23) and (24)
$I_{1,2}$ = convenient notations to simplify Eqs. (23) and (24)
$J_{1,2}$ = convenient notations to simplify Eqs. (23) and (24)
$R_{x,y}$ = principal relative radii of curvature in x, y direction (m); $\frac{R_{x,y_1}\cdot R_{x,y_2}}{R_{x,y_1}+R_{x,y_2}}$
$R_{x,y_{1,2}}$ = surface principal radii of curvature in x, y direction of bodies 1 and 2 (m)
T_0 = lubricant reference temperature (°C)
$T_{1,2}$ = surface temperatures (°C)
$T_{1,2i,j}$ = surface temperatures of bodies 1 and 2 at node i, j (°C)
$T_{avgi,j}$ = average temperature at node i, j (°C)
$T_{b_{1,2}}$ = bulk temperatures of bodies 1 and 2 (°C)
$T_{fi,j,m}$ = temperature distribution along the film thickness at node i, j and fraction m (°C)
$h_0^{(s)}$ = current iteration normal approach (m)
$h_0^{(s+1)}$ = updated normal approach (m)
$p_{k,l}^{(s)}$ = current pressure distribution acting at node k, l (Pa)
$p_{k,l}^{(s+1)}$ = updated pressure distribution acting at node k, l (Pa)
$\hat{p}_{k,l}^{(s+1)}$ = updated pressure distribution acting at node k, l in the auxiliary matrix (Pa)
$p_{k,l_{\mathrm{Reynolds}}}^{(s)}$ = pressure obtained from Reynolds equation (Pa)
$A_{i,j}^{(s)}$ = coefficient matrix for $p_{i-1,j}^{(s+1)}$ at iteration index (s)
$B_{i,j}^{(s)}$ = coefficient matrix for $p_{i,j}^{(s+1)}$ at iteration index (s)
$C_{i,j}^{(s)}$ = coefficient matrix for $p_{i+1,j}^{(s+1)}$ at iteration index (s)
$D_{k,l}^{i,j}$ = coefficient of influence matrix
$h \equiv h(x, y)$ = film thickness between bodies 1 and 2 (m)
$p \equiv p(x, y)$ = pressure distribution (Pa)
$p(x', y')$ = pressure applied at the point (x', y')(Pa)
$s_{1,2}(x, y)$ = surface roughness amplitude of bodies 1 and 2 (m)
$u_z(x, y)$ = pressure-induced elastic displacement at the point (x, y) (m)
$(u_z)_{i,j}$ = numerical displacement at node i, j (m)
$(u_z)_{i,j}^e$ = elastic displacement at node i, j (m)
$(u_z)_{i,j}^{ep}$ = elastoplastic displacement at node i, j (m)
$(u_z)_{i,j}^p$ = plastic deformation at node i, j (m)
x, y = coordinates (x is chosen to be parallel to the rolling direction) (m)
C_a, C_b = coefficients for pressure–density equation $C_a = 0.6\times 10^{-9}$ $C_b = 1.7\times 10^{-9}$
$N_x = N_y$ = mesh node number
SRR = Slide-to-Roll Ratio $\frac{|\mathbf{v}_2-\mathbf{v}_1|}{\|\mathbf{v}_\mathrm{e}\|}$
α_{Gold} = pressure-viscosity coefficient calculated by Gold's formula (Pa^{-1})
α_k = relaxation factor used to update the pressure
α_τ, β_τ = lubricant limiting yield shear stress constants
$\alpha_\mathrm{G}, \beta_\mathrm{G}$ = lubricant limiting elastic shear modulus constants
β = temperature-viscosity coefficient (K^{-1})
γ_t = oil thermal expansion coefficient (°C^{-1})
$\dot{\gamma}$ = lubricant shear strain rate (s^{-1})
$\Delta x = \Delta y$ = mesh grid size (m)
Δh = normal approach increment (m)
$\delta_{i,j}^{(s)}$ = coefficient matrix agglutinating known values at the iteration index (s)
$\varepsilon_{i,j}^{x,y}$ = convenient notations to simplify Eq. (10)
η = lubricant dynamic viscosity at a given pressure (Pa·s)
η_T = lubricant dynamic viscosity at atmospheric pressure and temperature (Pa·s)
θ = angle between $\mathbf{v}_2$ and $\mathbf{v}_1$
$\nu_{1,2}$ = Poisson's Ratio of bodies 1 and 2
ρ = lubricant density at a given pressure (kg/m^3)
ρ_T = lubricant density at atmospheric pressure and given temperature (kg/m^3)
ρ_0 = lubricant density at atmospheric pressure and reference temperature (kg/m^3)
$\rho_{1,2}$ = density at atmospheric pressure and temperature of bodies 1 and 2 (kg/m^3)
τ = the lubricant shear stress (Pa)
τ_L = lubricant limiting yield shear stress (Pa)
φ_e = entrainment velocity angle
$\phi_{i,j}$ = convenient notation to simplify Eq. (11)
ω_d = sample disc angular velocity (rad/s)
ξ, ζ, ψ = lubricant constants for Voguel equation

Appendix A1

The steady-state Reynolds equation used to describe circular contact is presented in Eq. (1). By discretizing the problem using a rectangular grid of uniform mesh size in each direction ($\Delta x = \Delta y$), one can write Eqs. (10) and (11), where the convenient notations $\varepsilon_{i,j}^{x,y}$ are detailed in Eqs. (A1)–(A5)

$$\varepsilon^{x}_{i,j} = \varepsilon^{y}_{i,j} = \frac{\rho_{i,j} \cdot h^{3}_{i,j}}{12 \cdot \eta_{i,j} \cdot \|\mathbf{v}_e\|} \tag{A1}$$

$$\varepsilon^{x}_{i-\frac{1}{2},j} = \frac{\varepsilon^{x}_{i,j} + \varepsilon^{x}_{i-1,j}}{2} \tag{A2}$$

$$\varepsilon^{x}_{i+\frac{1}{2},j} = \frac{\varepsilon^{x}_{i,j} + \varepsilon^{x}_{i+1,j}}{2} \tag{A3}$$

$$\varepsilon^{y}_{i,j-\frac{1}{2}} = \frac{\varepsilon^{y}_{i,j} + \varepsilon^{y}_{i,j-1}}{2} \tag{A4}$$

$$\varepsilon^{y}_{i,j+\frac{1}{2}} = \frac{\varepsilon^{y}_{i,j} + \varepsilon^{y}_{i,j+1}}{2} \tag{A5}$$

Appendix A2

The Coefficient of Influence Matrix ($D^{i,j}_{k,l}$) depends only on the geometric mesh structure. With the zero-order approximation, pressure is assumed to be constant in each rectangular mesh element, so an analytical solution of Eq. (3) can be found [21]. Equations (B1)–(B5) present the Coefficient of Influence Matrix

$$\begin{aligned} D^{i,j}_{k,l} = {} & x_p \cdot \ln\left(y_p + \sqrt{x_p^2 + y_p^2}\right) \\ & + y_p \cdot \ln\left(x_p + \sqrt{x_p^2 + y_p^2}\right) + x_m \cdot \ln\left(y_m + \sqrt{x_m^2 + y_m^2}\right) \\ & + y_m \cdot \ln\left(x_m + \sqrt{x_m^2 + y_m^2}\right) - x_m \cdot \ln\left(y_p + \sqrt{x_m^2 + y_p^2}\right) - y_p \\ & \cdot \ln\left(x_m + \sqrt{x_m^2 + y_p^2}\right) - x_p \cdot \ln\left(y_m + \sqrt{x_p^2 + y_m^2}\right) \\ & - y_p \cdot \ln\left(x_p + \sqrt{x_p^2 + y_m^2}\right) \end{aligned} \tag{B1}$$

$$x_p = |x_i - x_k| + \frac{\Delta x}{2} \tag{B2}$$

$$x_m = |x_i - x_k| - \frac{\Delta x}{2} \tag{B3}$$

$$y_p = |y_j - y_l| + \frac{\Delta y}{2} \tag{B4}$$

$$y_m = |y_j - y_l| - \frac{\Delta y}{2} \tag{B5}$$

Appendix A3

As indicated by Wang et al. [7], following the discretization of the Poiseuille and Couette flow terms, a system of linear equations with unknown pressures is obtained. By assuming $p_{i,j}$, $p_{i+1,j}$, and $p_{i-1,j}$ as the unknown variables and moving the terms related to $p_{i,j-1}$ and $p_{i,j+1}$ to the right-hand side, the discrete Reynolds equation can be solved. The form of the linear equation set is presented in Eq. (12) for the iteration index (s) [7]. Equations (C1)–(C4) present the required terms

$$A^{(s)}_{i,j} = \varepsilon^{x(s)}_{i-\frac{1}{2},j} - (\rho^{(s)}_{i,j} \cdot D^{i,j}_{i-1,j} - \rho^{(s)}_{i-1,j} \cdot D^{i-1,j}_{i-1,j})\Delta x \tag{C1}$$

$$B^{(s)}_{i,j} = -\left(\varepsilon^{x(s)}_{i-\frac{1}{2},j} + \varepsilon^{x(s)}_{i+\frac{1}{2},j} + \varepsilon^{y(s)}_{i,j-\frac{1}{2}} + \varepsilon^{y(s)}_{i,j+\frac{1}{2}}\right) - (\rho^{(s)}_{i,j} \cdot D^{i,j}_{i,j} - \rho^{(s)}_{i-1,j} \cdot D^{i-1,j}_{i,j})\Delta x \tag{C2}$$

$$C^{(s)}_{i,j} = \varepsilon^{x(s)}_{i+\frac{1}{2},j} - (\rho^{(s)}_{i,j} \cdot D^{i,j}_{i+1,j} - \rho^{(s)}_{i-1,j} \cdot D^{i-1,j}_{i+1,j})\Delta x \tag{C3}$$

$$\begin{aligned} \delta^{(s)}_{i,j} = {} & -\left(\varepsilon^{y(s)}_{i,j-\frac{1}{2}} \cdot p^{(s)}_{i,j-1} + \varepsilon^{y(s)}_{i,j+\frac{1}{2}} \cdot p^{(s)}_{i,j+1}\right) + [\cos(\varphi_e) \cdot \left(\rho^{(s)}_{i,j} \cdot h^{(s)}_{i,j} - \rho^{(s)}_{i-1,j} \cdot h^{(s)}_{i-1,j}\right) \\ & + \sin(\varphi_e) \cdot \left(\rho^{(s)}_{i,j} \cdot h^{(s)}_{i,j} - \rho^{(s)}_{i,j-1} \cdot h^{(s)}_{i,j-1}\right) - \left(\rho^{(s)}_{i,j} \cdot D^{i,j}_{i,j} - \rho^{(s)}_{i-1,j} \cdot D^{i-1,j}_{i,j}\right) \\ & p^{(s)}_{i,j} - (\rho^{(s)}_{i,j} \cdot D^{i,j}_{i-1,j} - \rho^{(s)}_{i-1,j} \cdot D^{i-1,j}_{i-1,j}) p^{(s)}_{i-1,j} - \left(\rho^{(s)}_{i,j} \cdot D^{i,j}_{i+1,j} - \rho^{(s)}_{i-1,j} \cdot D^{i-1,j}_{i+1,j}\right) \\ & p^{(s)}_{i+1,j}] \cdot \Delta x \end{aligned} \tag{C4}$$

Appendix A4

Calculating T_1 and T_2 requires a division of the solution domain into many differential strips. The discretized equations used in the temperature calculation are shown in Eqs. (23) and (24). The convenient notation G_1, G_2, I_1, I_2, J_1, and J_2 are detailed in Eqs. (D1)–(D6)

$$G_1 = \left(\frac{1}{\pi \cdot \rho_1 \cdot C_1 \cdot \|\vec{v}_1\| \cdot k_1}\right)^{0.5} \cdot \frac{\sqrt{\Delta x}}{2} \tag{D1}$$

$$G_2 = \left(\frac{1}{\pi \cdot \rho_2 \cdot C_2 \cdot \|\mathbf{v}_2\| \cdot \cos(\theta) \cdot k_2}\right)^{0.5} \cdot \frac{\sqrt{\Delta x}}{2} \tag{D2}$$

$$\begin{aligned} I_1 = {} & \left(\frac{1}{\pi \cdot \rho_1 \cdot C_1 \cdot \|\mathbf{v}_1\| \cdot k_1}\right)^{0.5} \cdot \frac{k_{f\,i,j}}{h_{i,j}} \\ & \cdot \left\{\sum_{k=0}^{i}\left[\omega_k \cdot \frac{T_{2k,j} - T_{1k,j}}{(x_{i+1} - x_k)^{0.5}} \cdot \Delta x + (T_{2i,j} - T_{1i,j}) \cdot \sqrt{\Delta x}\right]\right\} \\ & + \frac{C_1}{2} \cdot \left\{\sum_{k=0}^{i}\left[\omega_k \cdot \frac{q_{k,j} \cdot \Delta x}{(x_{i+1} - x_k)^{0.5}}\right] + q_{i,j} \cdot \sqrt{\Delta x}\right\} + T_{b_1\,i,j} \end{aligned} \tag{D3}$$

$$\begin{aligned} I_2 = {} & \left(\frac{1}{\pi \cdot \rho_2 \cdot C_2 \cdot \|\mathbf{v}_2\| \cdot \cos(\theta) \cdot k_2}\right)^{0.5} \cdot \frac{k_{f\,i,j}}{h_{i,j}} \\ & \cdot \left\{\sum_{k=0}^{i}\left[\omega_k \cdot \frac{T_{1k,j} - T_{2k,j}}{(x_{i+1} - x_k)^{0.5}} \cdot \Delta x + (T_{1i,j} - T_{2i,j}) \cdot \sqrt{\Delta x}\right]\right\} \\ & + \frac{C_2}{2} \cdot \left\{\sum_{k=0}^{i}\left[\omega_k \cdot \frac{q_{k,j} \cdot \Delta x}{(x_{i+1} - x_k)^{0.5}}\right] + q_{i,j} \cdot \sqrt{\Delta x}\right\} + T_{b_2\,i,j} \end{aligned} \tag{D4}$$

$$J_1 = \left(\frac{1}{\pi \cdot \rho_1 \cdot C_1 \cdot \|\mathbf{v}_1\| \cdot k_1}\right)^{0.5} \cdot \frac{k_{f\,i,j} \cdot \sqrt{\Delta x}}{h_{i,j}} \tag{D5}$$

$$J_2 = \left(\frac{1}{\pi \cdot \rho_2 \cdot C_2 \cdot \|\mathbf{v}_2\| \cdot \cos(\theta) \cdot k_2}\right)^{0.5} \cdot \frac{k_{f\,i,j} \cdot \sqrt{\Delta x}}{h_{i,j}} \tag{D6}$$

where ω_k are the weighting coefficients for the specific numerical integration method employed. In this work, the composite trapezoidal rule was used, which means that the first and last ω_k are equal to 0.5, while the remaining weighting coefficients are equal to 1.0.

Appendix A5

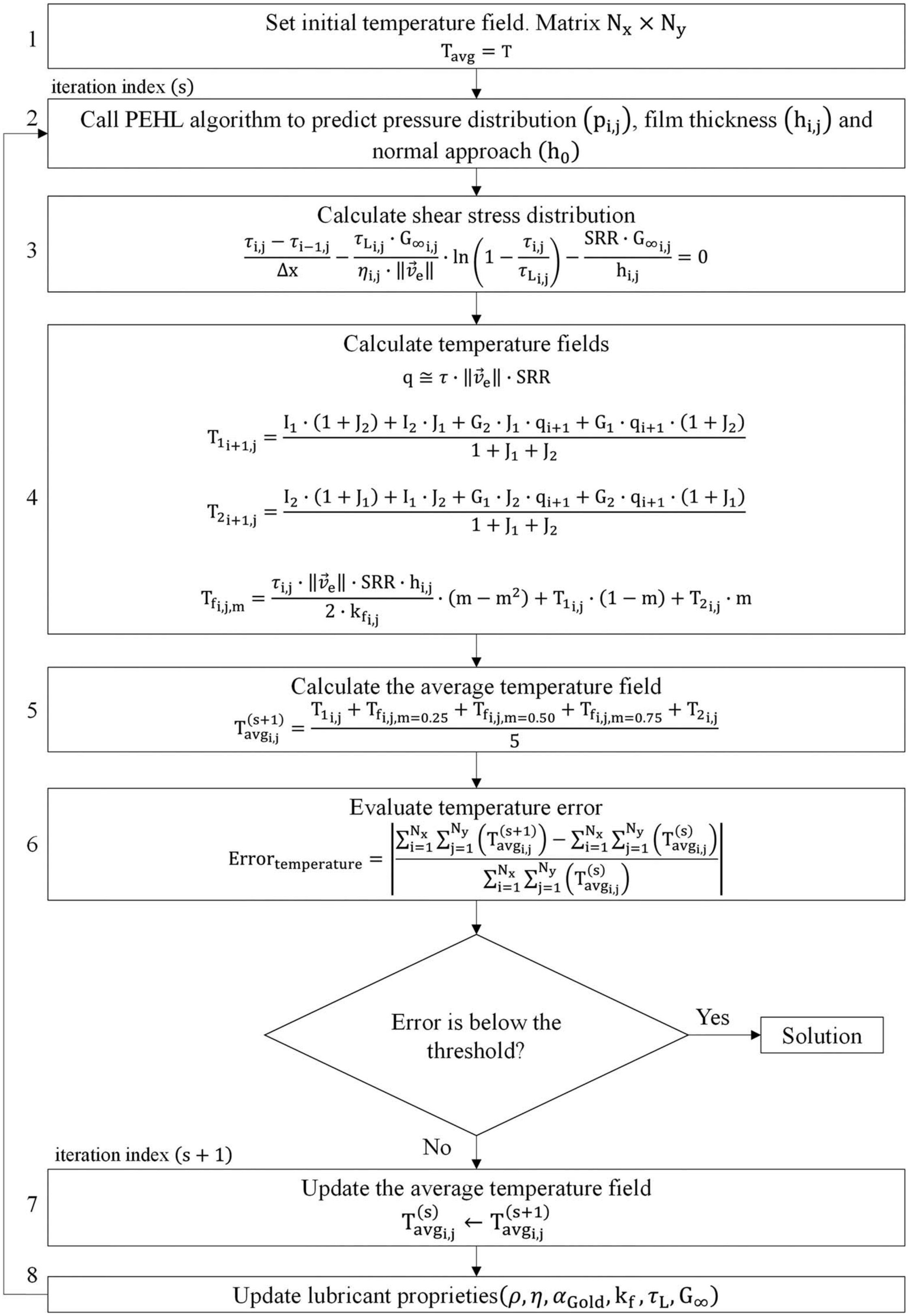

Fig. 13 Algorithm for solving TPEHL circular contact

Appendix A6

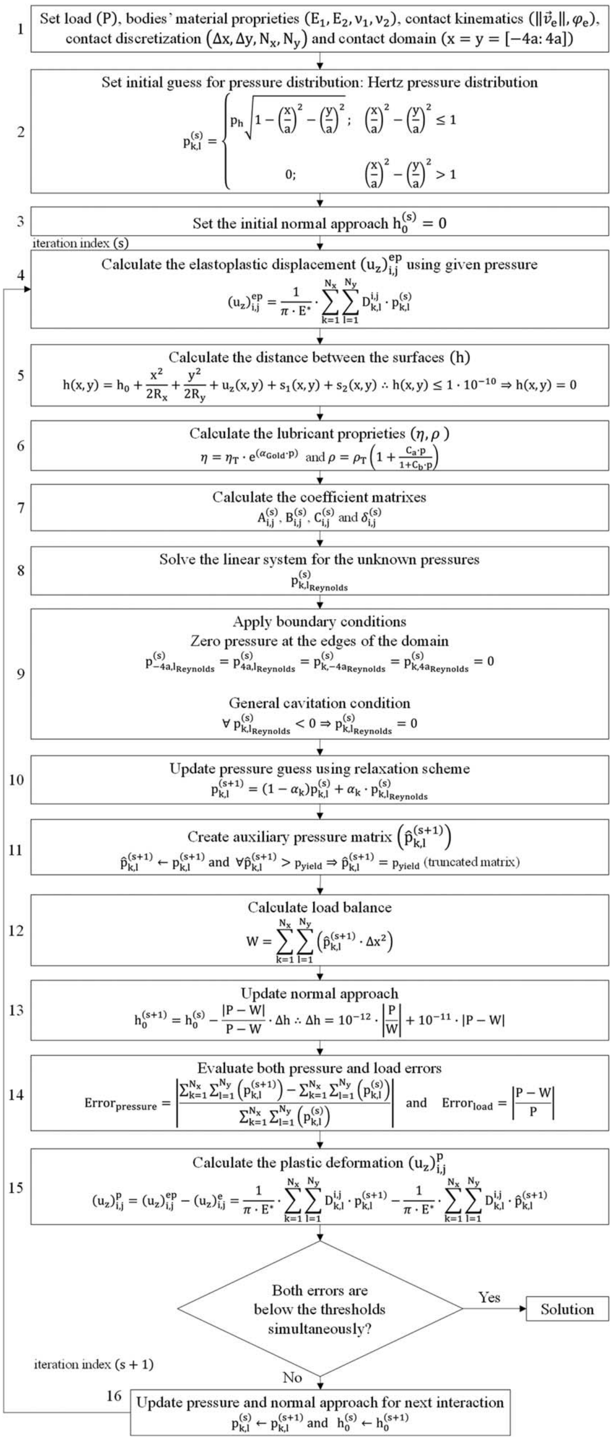

Fig. 14 Algorithm for solving PEHL circular contact

References

[1] Wang, X., Liu, Y., and Zhu, D., 2017, "Numerical Solution of Mixed Thermal Elastohydrodynamic Lubrication in Point Contacts With Three-Dimensional Surface Roughness," ASME J. Tribol., **139**(1), p. 011501.

[2] He, T., Ren, N., Zhu, D., and Wang, J., 2014, "Plasto-Elastohydrodynamic Lubrication in Point Contacts for Surfaces With Three-Dimensional Sinusoidal Waviness and Real Machined Roughness," ASME J. Tribol., **136**(3), p. 031504.

[3] Hamrock, B., and Dowson, D., 1977, "Isothermal Elastohydrodynamic Lubrication of Point Contacts: Part III—Fully Flooded Results," ASME J. Lubr. Technol., **99**(2), pp. 264–275.

[4] Venner, C., and Lubrecht, A., 1996, "Numerical Analysis of the Influence of Waviness on the Film Thickness of a Circular EHL Contact," ASME J. Tribol., **118**(1), pp. 153–161.

[5] Zhu, D., and Ai, X., 1997, "Point Contact EHL Based on Optically Measured Three-Dimensional Rough Surfaces," ASME J. Tribol, **119**(3), pp. 375–384.

[6] Hu, Y.-Z., and Zhu, D., 2000, "A Full Numerical Solution to the Mixed Lubrication in Point Contacts," ASME J. Tribol., **122**(1), pp. 1–9.

[7] Wang, Y., Dorgham, A., Liu, Y., Wang, C., Wilson, M., Neville, A., and Azam, A., 2021, "An Assessment of Quantitative Predictions of Deterministic Mixed Lubrication Solvers," ASME J. Tribol., **143**(1), p. 011601.

[8] Ren, N., Zhu, D., Chen, W., and Wang, Q., 2010, "Plasto-Elastohydrodynamic Lubrication (PEHL) in Point Contacts," ASME J. Tribol., **132**(3), p. 031501.

[9] Zhu, D., and Wen, S., 1984, "A Full Numerical Solution for the Thermoelastohydrodynamic Problem in Elliptical Contacts," ASME J. Tribol., **106**(2), pp. 246–254.

[10] Wang, W.-Z., Liu, Y.-C., Wang, H., and Hu, Y.-Z., 2004, "A Computer Thermal Model of Mixed Lubrication in Point Contacts," ASME J. Tribol., **126**(1), pp. 162–170.

[11] Pu, W., Wang, J., and Zhu, D., 2016, "Friction and Flash Temperature Prediction of Mixed Lubrication in Elliptical Contacts With Arbitrary Velocity Vector," Tribol. Int., **99**(1), pp. 38–46.

[12] Azam, A., Dorgham, A., Morina, A., Neville, A., and Wilson, M., 2019, "A Simple Deterministic Plastoelastohydrodynamic Lubrication (PEHL) Model in Mixed Lubrication," Tribol. Int., **131**(1), pp. 520–529.

[13] He, T., Zhu, D., Wang, J., and Wang, J. Q., 2017, "Experimental and Numerical Investigations of the Stribeck Curves for Lubricated Counterformal Contacts," ASME J. Tribol., **139**(2), p. 021505.

[14] Zhu, D., Wang, J., and Jane Wang, Q., 2015, "On the Stribeck Curves for Lubricated Counterformal Contacts of Rough Surfaces," ASME J. Tribol., **137**(2), p. 021501.

[15] Chittenden, R., Dowson, D., Dunn, J., and Taylor, C., 1985, "A Theoretical Analysis of the Isothermal Elastohydrodynamic Lubrication of Concentrated Contacts. II. General Case, With Lubricant Entrainment Along Either Principal Axis of the Hertzian Contact Ellipse or at Some Intermediate Angle," Proc. R. Soc. Lond. A, **397**(1813), pp. 271–294.

[16] Johnson, L., 1985, *Contact Mechanics*, 1th ed., Cambridge University Press, Cambridge.

[17] Dowson, D., and Higginson, R., 1977, *Elasto-Hydrodynamic Lubrication, (International Series on Materials Science and Technology, Vol. 23*, Pergamon, Oxford, UK.

[18] Barus, C., 1893, "Isothermals, Isopiestics and Isometrics Relative to Viscosity," Am. J. Sci., **45**(266), pp. 87–96.

[19] Gohar, R., and Safa, M., 2010, *Tribology and Dynamics of Engine and Powertrain*, Woodhead Publishing, Sawston, UK, pp. 132–170.

[20] Gold, P., Schmidt, A., Dicke, H., Loos, J., and Assmann, C., 2006, "Viscosity–Pressure–Temperature Behaviour of Mineral and Synthetic Oils," J. Synth. Lubr., **18**(1), pp. 51–79.

[21] Wang, Q., and Zhu, D., 2019, *Interfacial Mechanics: Theories and Methods for Contact and Lubrication*, 1st ed., CRC Press Taylor & Francis Group, LLC, Boca Raton, FL.

[22] Bair, S., and Winer, W., 1979, "A Rheological Model for Elastohydrodynamic Contacts Based on Primary Laboratory Data," ASME J. Lubr. Technol., **101**(3), pp. 258–264.

[23] Brandão, J. A., Meheux, M., Seabra, J. H. O., Ville, F., and Castro, M. J. D., 2011, "Traction Curves and Rheological Parameters of Fully Formulated Gear Oils," Proc. Inst. Mech. Eng. J: J. Eng. Tribol., **225**(7), pp. 577–593.

[24] Meziane, B., Vergne, P., Devaux, N., Lafarge, L., Morales-Espejel, G., and Fillot, N., 2020, "Film Thickness Build-Up in Zero Entrainment Velocity Wide Point Contacts," Tribol. Int., **141**, p. 105897.

[25] Gama, A., Cousseau, T., Graça, B., Castro, J., and Seabra, J., 2016, "Experimental Measuring Set-Up and Procedure for the Traction Coefficient on Roller-On-Disc Contact," Lubr. Sci., **28**(6), pp. 349–362.